CHEMPLUSCHEM
FULL PAPERS

ChemPubSoc Europe

DOI: 10.1002/cplu.201300147

SPECIAL ISSUE

Activation of Methane by Os^+: Guided-Ion-Beam and Theoretical Studies

P. B. Armentrout,*[a] Laura Parke,[a] Christopher Hinton,[a, b] and Murat Citir[a, c]

In memory of Detlef Schröder

Activation of methane by the third-row transition-metal cation Os^+ is studied experimentally by examining the kinetic energy dependence of reactions of Os^+ with CH_4 and CD_4 using guided-ion-beam tandem mass spectrometry. A flow tube ion source produces Os^+ in its electronic ground state and primarily in the ground spin–orbit level. Dehydrogenation to form $[Os,C,2H]^+ + H_2$ is exothermic, efficient, and the only process observed at low energies for reaction of Os^+ with methane, whereas OsH^+ dominates the product spectrum at higher energies. The kinetic energy dependences of the cross sections for several endothermic reactions are analyzed to give 0 K bond dissociation energies (in eV) of $D_0(Os^+–C) = 6.20 \pm 0.21$, $D_0(Os^+–CH) = 6.77 \pm 0.15$, and $D_0(Os^+–CH_3) = 3.00 \pm 0.17$. Because it is formed exothermically, $D_0(Os^+–CH_2)$ must be greater than 4.71 eV, and a speculative interpretation suggests the exothermicity exceeds 0.6 eV. Quantum chemical calculations at the B3LYP/def2-TZVPP level show reasonable agreement with the experimental bond energies and with previous theoretical values available. Theory also provides the electronic structures of the product species as well as intermediates and transition states along the reactive potential energy surfaces. Notably, the structure of the dehydrogenation product is predicted to be $HOsCH^+$, rather than $OsCH_2^+$, in contrast to previous work.

Introduction

Methane, a major component of natural gas, is the least reactive hydrocarbon and therefore its functionalization presents a major technical challenge and opportunity. Catalysts for direct conversion of methane to either methanol or ethene would be of great technological interest. To develop more efficient and economical homogeneous catalysts for such purposes, an understanding of the various factors that contribute to the activation of the inert CH bonds of methane is needed. For this purpose, gas-phase studies are a good starting point for providing information on the intrinsic properties of metals in the absence of solvent, stabilizing ligands, and metal supports. Schwarz has reviewed such studies specifically with regard to methane activation,[1] and Roithová and Schröder have examined the broader range of CH bond activation in the gas phase.[2] Such studies also form an ideal interface for theoretical calculations on such complicated elements, thus providing benchmark information to guide theory of more complex systems.

[a] *Prof. P. B. Armentrout, L. Parke, Dr. C. Hinton, Dr. M. Citir*
Chemistry Department
University of Utah
315 S. 1400 E. Rm. 2020, Salt Lake City, UT 84112 (USA)
E-mail: armentrout@chem.utah.edu

[b] *Dr. C. Hinton*
Present address: Institute for Scientific Research
Boston College, Chestnut Hill, MA 02467 (USA)

[c] *Dr. M. Citir*
Present address: Abdullah Gül University
Melikgazi/Kayseri 38039 (Turkey)

Supporting information for this article is available on the WWW under http://dx.doi.org/10.1002/cplu.201300147.

Considerable research has been done to study the reactions of the first-row and second-row transition-metal ions (M^+) with hydrogen and small hydrocarbons in the gas phase.[1–11] Among the experimental techniques available for measuring the thermodynamics of gas-phase species, the guided-ion-beam method used in our laboratory can examine reactions at hyperthermal energies, and thereby has the ability to study endothermic reactions. This permits the determination of the bond dissociation energies (BDEs) for $M^+–C_xH_y$ ($x = 0–3$, $y = 0–2x + 2$). The thermochemistry obtained from these studies is of clear fundamental interest and is relevant to a variety of catalytic reactions involving transition-metal systems.[12,13] Such ion-beam studies also provide insight into the electronic requirements for the activation of methane by transition-metal ions. We have applied this methodology to all the first-row and second-row transition metals except Tc[14–26] and more recently to all of the third-row metals except Os as well.[25,27–34] A significant advantage of these comprehensive studies is the comparison of bond energies and reactivities of all transition-metal complexes, thereby establishing periodic trends. A particularly interesting feature of the third-row transition metals is the study of the influence of strong spin–orbit coupling on the reactivity. Similar factors are undoubtedly at work in reactions of the lanthanides and actinide cations, which have been studied primarily at thermal energies.[35–39]

Herein, we report results for the reactions of Os^+ with CH_4 and CD_4 over a wide range of kinetic energies. In previous work on this system, Irikura and Beauchamp used a Fourier transform ion cyclotron resonance (FTICR) spectrometer and found that Os^+ dehydrogenates CH_4 with $(35 \pm 9)\%$ efficiency

at room temperature.[40] In flow tube studies,[41] Bohme and coworkers found this reaction occurs with (94±28)% efficiency. In both cases, the reactivity of Os^+ is second only to Ir^+, which reacted with unit efficiency in the flow tube studies and (71±18)% in the FTICR study. In the present work, we examine this exothermic reaction as well as all endothermic processes, thereby probing the potential energy surfaces, providing mechanistic information complementary to previous experimental and theoretical work, and yielding the first thermodynamic information regarding these processes. Theoretical calculations are also performed to assign electronic structures and explore potential energy surfaces and possible mechanisms. These are compared with previous results,[40,42–44] in particular, the theoretical studies of Zhang, Li, and Jiang (ZLJ)[45] who examined the potential energy surface for the dehydrogenation of methane by Os^+. Notably, several new features in these surfaces are elucidated here; most importantly, the likely ground-state structure of the dehydrogenation product is $HOsCH^+$ rather than $OsCH_2^+$ and formation of this product proceeds through an osmium trihydride carbyne cation intermediate, H_3OsCH^+. Evidence for the $HOsCH^+$-type structure has recently been obtained spectroscopically in the related iridium cation system.[46]

Results

Guided-ion-beam results for reaction of Os^+ with methane

Figure 1 shows cross sections for the reaction of Os^+ with CD_4, which yields product ions as shown in reactions (1)–(5):

$$Os^+ + CD_4 \rightarrow OsD^+ + CD_3 \quad (1)$$

$$\rightarrow OsCD_3^+ + D \quad (2)$$

$$\rightarrow OsCD_2^+ + D_2 \quad (3)$$

$$\rightarrow OsCD^+ + D + D_2 \quad (4)$$

$$\rightarrow OsC^+ + 2\,D_2 \quad (5)$$

The additional product observed, $OsC_2D_4^+$, must clearly come from sequential reactions with CD_4 and can be assigned to reaction (6):

$$OsCD_2^+ + CD_4 \rightarrow OsC_2D_4^+ + D_2 \quad (6)$$

Studies of the reaction of Os^+ with CH_4 were also performed (shown in Figure S1 in the Supporting Information) and yielded results consistent with those shown in Figure 1. Results from the perdeuterated species are presented here because CD_4 reduces mass overlap and allows the intensities of the various product ions to be measured more accurately and, in particular, permits differentiation of the very weak $OsCD_3^+$ signal from the much more intense $OsCD_2^+$ signal.

As can be seen from Figure 1, dehydrogenation to form $OsCD_2^+ + D_2$ is the only primary process observed at low energies, consistent with previous studies at thermal energies.[40,41] The cross section for dehydrogenation of CD_4 to produce $OsCD_2^+$ decreases with increasing energy, thus indicating an

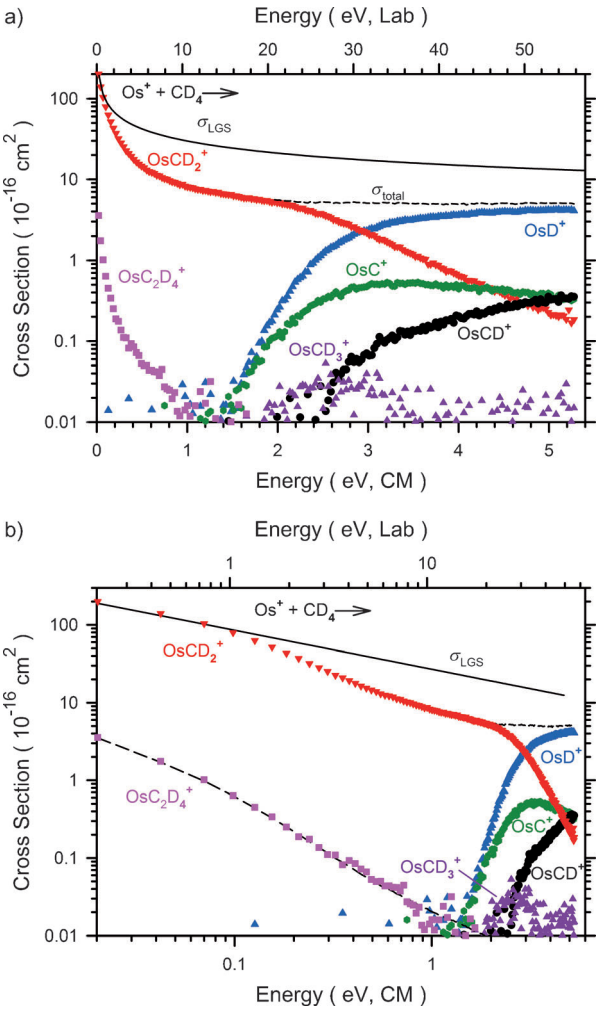

Figure 1. Cross sections for reaction of Os^+ (^6D) with CD_4 as a function of kinetic energy in the center-of-mass (CM) frame (lower axis) and laboratory (Lab) frame (upper axis). The solid line shows the Langevin–Gioumousis–Stevenson (LGS) collision cross section, the short-dashed line shows the total cross section, and the long-dashed line in (b) shows the cross section for $OsCD_2^+$ multiplied by $E^{-1/2}$ and scaled down by 400.

exothermic reaction having no barrier in excess of the energy of the reactants. This reaction cross section declines approximately as $E^{-0.5\pm0.1}$ below 0.1 eV, comparable to the prediction of the Langevin–Gioumousis–Stevenson (LGS) collision cross section, σ_{LGS},[47] which has an $E^{-1/2}$ energy dependence. The magnitudes of the experimental and LGS collision cross sections are the same, well within the ±20% uncertainty in the absolute magnitudes. To compare the reaction efficiency measured here with previous results, our cross section is converted to a rate coefficient by the following expression, $k(<E>) = v\sigma(E)$, in which $v = (2E/\mu)^{1/2}$ and $\mu = mM/(m+M)$, the reduced mass of the reactants. The rate coefficients depend on the mean energy of the reactants, which includes the average thermal motion of the neutral, such that $<E> = E + (3/2)\gamma k_B T$, in which $\gamma = M/(m+M)$. As discussed previously,[48] the rate $k(<E>)$ has the property that it approaches the thermal rate coefficient for the effective temperature $T' = \gamma T$, which equals 277 K (272 K for CD_4) for the present results, as $v \rightarrow 0$. By using these equations, we obtain $k = (10.2\pm2.0)\times10^{-10}$ cm^3 s^{-1} for

reaction with CH_4 and $k=(8.4\pm1.7)\times10^{-10}$ cm^3s^{-1} for reaction with CD_4. These values are higher than literature rate constants obtained by ICR mass spectrometry of $(3.4\pm0.9)\times10^{-10}$ cm^3s^{-1} for CH_4,[40] but are in good agreement with the value of $(9.2\pm2.8)\times10^{-10}$ cm^3s^{-1} obtained in flow tube measurements.[41] Compared to the LGS collision rate, we find the reactions with CH_4 and CD_4 occur with efficiencies of (104 ± 20) and (95 ± 19)%, respectively, again consistent with the flow tube results of (94 ± 28)%, but higher than the ICR results of (35 ± 9)%.[40] A similar discrepancy was found previously for the dehydrogenation of CH_4 by Ir^+, the most reactive third-row metal cation. We found that this process occurs with unit efficiency,[32] as did the flow tube studies of Bohme and co-workers,[41] whereas the ICR results find an efficiency of 71%.[40] One possible explanation for these observations is that the ICR results occurred for ions that are not completely thermalized, which would then reduce the reaction efficiency, as shown in Figure 1 for Os^+.

Reaction (6), the sequential reaction of the $OsCD_2^+$ product, has also been observed before by Irikura and Beauchamp; however, they do not report a rate constant.[49] We find that the energy dependence of this cross section matches that of $\sigma(OsCD_2^+)\times E^{-1/2}$, as shown in Figure 1b. This is the behavior expected for $OsCD_2^+$ reacting according to the LGS collision model, thus indicating that reaction (6) is barrierless and exothermic.

Between energies of 0.2 and 2.0 eV, the $OsCD_2^+$ (and $OsCH_2^+$) cross sections decline as $E^{-0.9\pm0.1}$. Some of this behavior can be attributed to conservation of angular momentum, which greatly favors a return to reactants compared to formation of the products, because the reduced mass and polarizability of the products are much lower than those of the reactants, as discussed previously.[50] In essence, the centrifugal barrier to reaction in the product channel increases much more rapidly than in the entrance channel such that collisions at large impact parameters can no longer conserve angular momentum while forming products, and hence they are forced to return to reactants. We modeled this behavior using a phase space approach in which angular momentum is explicitly conserved. This model requires knowledge of the exothermicity of the dehydrogenation reaction as this controls the energy range over which deviations from σ_{LGS} are observed. If the exothermicity of the reaction exceeds 0.6 eV, the phase space model cross section deviates from σ_{LGS} starting at approximately 0.1 eV (as observed experimentally); however, quantitative agreement with the experimental results could not be found for any set of reasonable parameters because the experimental cross section declines more rapidly with energy (see Figure S1 for an example). To reproduce the data with good fidelity, the phase space model can be combined with a Landau–Zener (LZ) model for the energy dependence of crossing between adiabatic potential energy surfaces.[51] We have shown that this can be parameterized as $P_{LZ}=[c/(E-E_c)]^{-1/2}$ whether the system makes a single or multiple passes through the crossing region.[52] Here, c is a surface coupling term that depends on the energy gap between the adiabatic curves and inversely on the difference in the slopes of the diabatic curves at the crossing point, E is the relative kinetic energy of the reactants, and E_c is the potential energy of the crossing point. Note that the combination of $\sigma_{LGS}\times P_{LZ}$ predicts an approximate E^{-1} energy dependence, as observed experimentally above 0.2 eV. The best agreement between experiment and the phase space model combined with P_{LZ} utilized a value for E_c of about -0.25 eV, otherwise the model deviates from σ_{LGS} at the wrong energy (see Figure S1 for an example). Because of the complexities of this analysis and uncertainties in the parameters used, the >0.6 eV reaction exothermicity and -0.25 eV value of E_c obtained from this procedure are considered to be suggestive rather than definitive.

At still higher energies (>2 eV), the $OsCD_2^+$ (and $OsCH_2^+$) cross sections begin to decline more rapidly. There are four possible decomposition pathways that might account for this decline, which include decomposition into $OsC^+ + D_2$, $OsCD^+ + D$, $OsD^+ + CD$, and $Os^+ + CD_2$. The magnitudes of the cross sections for OsC^+ and $OsCD^+$ account for some of this decline, but not all of it. Decomposition of $OsCD_2^+$ to $Os^+ + CD_2$ and $OsD^+ + CD$ cannot begin until (4.82 ± 0.03) and (6.76 ± 0.10) eV, respectively,[27] too high to account for the decline. We therefore infer that the decrease in the $OsCD_2^+$ cross section must be attributable to competition with formation of $OsD^+ + CD_3$, which is consistent with the smooth energy dependence of the total cross section (Figure 1). Thus, these two product channels share a common intermediate, as discussed below.

Formation of $OsCD_3^+$ has a very small cross section near our sensitivity limit. This cross section peaks near 2.5 eV, close to the appearance of the $OsCD^+$ product. Thus, the formation of $OsCD_3^+$ is limited by its facile dissociation to $OsCD^+ + D_2$, a process that requires only (0.87 ± 0.24) eV according to the thermochemistry determined below.

OsC^+ product ions have a relatively low energy threshold, which indicates that they are formed by elimination of molecular deuterium from $OsCD_2^+$ [reaction (5)]. Other possible pathways for OsC^+ formation that stem from decomposition of either $OsCD_3^+$ or $OsCD^+$ require much higher energies than the dehydrogenation of $OsCD_2^+$, which requires $>(2.00\pm0.21)$ eV according to the thermochemical results below.

Thermochemical and theoretical results

The endothermic cross sections for each product ion are analyzed as described in the Experimental Section, and the optimum values of the parameters needed are listed in Table 1. Because this model explicitly includes rotational, translational, and vibrational energy distributions, all E_0 thresholds determined correspond to 0 K values. From the measured thresholds, the BDEs of the osmium–ligand cations can be calculated using Equation (7):

$$D_0(Os^+-L) = D_0(R-L)-E_0 \quad (7)$$

in which the D_0(R–L) values can be calculated using the heats of formation summarized previously.[27] This equation assumes that there are no activation barriers in excess of the endother-

Table 1. Optimized parameters for Equation (8) for $Os^+ + CH_4$ and CD_4 systems.

	Reaction	σ_0	n	E_0 [eV]	$D_0[Os^+–L]$ [eV]
$Os^+ + CH_4$	$\rightarrow OsH^+ + CH_3$	9.5 ± 2.0	1.0 ± 0.1	2.13 ± 0.04	2.35 ± 0.04
	$\rightarrow OsCH_2^+ + H_2$	–	–	< 0.0	> 4.71 ± 0.03
	$\rightarrow OsCH^+ + H_2 + H$	0.53 ± 0.16	1.1 ± 0.2	2.60 ± 0.24	6.47 ± 0.24
	$\rightarrow OsC^+ + 2H_2$	1.1 ± 0.3	0.9 ± 0.3	1.91 ± 0.15	6.15 ± 0.15
$Os^+ + CD_4$	$\rightarrow OsD^+ + CD_3$	13.5 ± 3.4	0.9 ± 0.1	2.28 ± 0.06	2.30 ± 0.06
	$\rightarrow OsCD_3^+ + D$	0.17 ± 0.03	1.9 ± 0.1	1.71 ± 0.15	2.87 ± 0.15
	$\rightarrow OsCD_2^+ + D_2$	–	–	< 0.0	> 4.82 ± 0.03
	$\rightarrow OsCD^+ + D_2 + D$	0.41 ± 0.08	1.5 ± 0.1	2.41 ± 0.08	6.84 ± 0.08
	$\rightarrow OsC^+ + 2D_2$	1.5 ± 0.4	1.3 ± 0.2	1.94 ± 0.15	6.26 ± 0.15

micity of a given reaction, an assumption that is often true for ion–molecule reactions because of the long-range attractive forces.[48,53] Table 2 provides a summary of the BDEs derived with structures for the ground-state species shown in Figure 2. Summaries of the B3LYP theoretical results (energies and detailed structural data) for each of the product ions and their excited states are provided in Tables S1 and S2 of the Supporting Information. These results are discussed in detail in the following sections for each species.

Os^+–H

We have recently measured a bond energy of (2.45 ± 0.10) eV for OsH^+ from the reactions of Os^+ with H_2 and D_2.[54] From Equation (7), D_0(D–CD_3) = 4.58 eV and a calculated zero-point energy difference between OsD^+ and OsH^+ of (0.039 ± 0.004) eV, this BDE predicts a threshold of (2.09 ± 0.10) eV for formation of OsD^+ in reaction (1). Our analysis of this cross section (Table 1) measures a somewhat higher threshold of (2.28 ± 0.06) eV, just outside of the combined experimental uncertainties. Similarly, the predicted E_0 value for the OsH^+ product ion obtained in the methane system is (2.03 ± 0.10) eV, whereas the measured threshold is (2.13 ± 0.04) eV, within experimental uncertainty. Thus, the CH_4 and CD_4 systems behave similarly to each other and their thresholds lead to a weighted average for $D_0(Os^+–H)$ = (2.32 ± 0.07) eV, for which the uncertainty is two standard deviations of the mean. This value lies (0.13 ± 0.12) eV below the thermodynamic results obtained from the H_2 and D_2 systems. Although similar to the combined experimental uncertainty, this discrepancy can be attributed to a competitive shift in which reaction (3) competes strongly with reaction (1) at its threshold, thereby delaying the apparent onset for formation of OsD^+ (OsH^+). In contrast, there are no competing channels in the reactions of Os^+ with H_2 and D_2, thus yielding what should be more reliable thermochemistry.

Generalized valence bond (GVB) calculations indicate that OsH^+ has a $^5\Pi$ ground state (GS) with a covalent bond formed between an sd hybridized (43% 6s and 56% 5d) orbital on Os^+ (^{6}D, 6s^{1}5d^6) and the 1s orbital on H.[55] These calculations find a 0 K BDE for OsH^+ of 2.44 eV, in excellent agreement with the experimental result.[54] Leininger et al. calculated the BDE of the $OsH^+(^5\Pi)$ state using RHF-MRCI and MCHF-SDCI levels of theory along with both small and large effective core potentials (ECPs) from Hay–Wadt, Christiansen and co-workers, and Stoll, Preuss, and co-workers.[56] The best agreement with our experimental value came from the small core ECPs, with 0 K BDEs in the range of 2.25–2.47 eV. Our own previous calculations found that BHLYP and CCSD(T) results were about 0.2 eV above the experiment, a difference that could be a result of the neglect of spin–orbit effects. Indeed, this is consistent with the spin–orbit corrections estimated below (see Experimental Section), which decrease the calculated bond energies by 0.36 − 0.19 = 0.17 eV. B3LYP results were higher than experiment by approximately

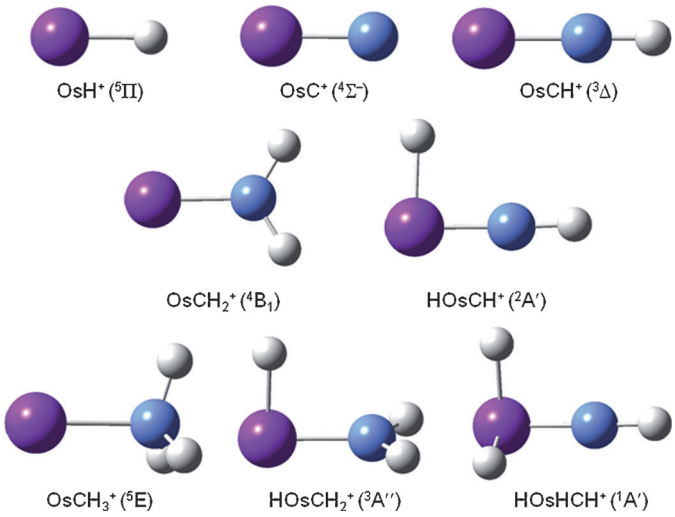

Figure 2. Structures of ground-state product ions formed during reaction of Os^+ with methane calculated at the B3LYP/def2-TZVPP level of theory.

Table 2. Comparison of experimental and theoretical 0 K bond energies (eV) for Os^+–H and Os^+–CH_x (x = 0–3) species.[a]

Species	State	This study						Previous study
		Expt.	Theory					Expt.
			B3LYP	BHLYP	BP86	QCISD[T]	CCSD[T]	
Os^+–H	$^5\Pi$	2.32 ± 0.07	2.91 (2.73)	2.64 (2.46)	3.15 (2.98)	2.77 (2.60)	2.77 (2.59)	2.45 ± 0.10[54]
Os^+–CH_3	^{5}E	2.87 ± 0.15	3.00 (2.83)	2.57 (2.39)	3.40 (3.23)	2.85 (2.67)	2.84 (2.67)	3.00 ± 0.19[b]
$HOsHCH^+$	^{1}A′		3.68 (3.32)	2.18 (1.82)	4.76 (4.40)	3.95 (3.59)	3.90 (3.54)	–
Os^+–CH_2	$^4B_1$	> 4.71	4.74 (4.37)	3.97 (3.61)	5.31 (4.95)	4.45 (4.09)	4.44 (4.07)	> 4.71[49]
$HOsCH^+$	^{2}A′	–	5.26 (4.90)	3.93 (3.57)	6.16 (5.80)	5.28 (4.91)	5.18 (4.81)	–
Os^+–CH	$^3\Delta$	6.77 ± 0.15	6.45 (6.46)	5.35 (5.36)	7.29 (7.30)	6.34 (6.35)	6.26 (6.27)	–
Os^+–C	$^4\Sigma^-$	6.20 ± 0.21	6.01 (5.65)	4.79 (4.43)	6.96 (6.59)	6.00 (5.63)	5.91 (5.55)	–
	$^2\Delta$		5.93 (5.94)	4.71 (4.73)	6.77 (6.79)	5.91 (5.92)	5.75 (5.77)	–
MAD[c]	–	–	0.4 (0.4)	1.0 (1.1)	0.9 (0.7)	0.5 (0.4)	0.5 (0.5)	–

[a] Calculations use the def2-TZVPP basis set on all elements. Values in parentheses have been approximately corrected for spin–orbit interactions. See text. [b] Bond energy adjusted as described in the text. [c] Mean absolute deviation from the best experimental results for OsH^+, OsC^+, $OsCH^+$, and $HOsHCH^+$.

0.4 eV, consistent with the results found by Holthausen et al. for the third-row transition-metal-ion methyl cations.[43] BP86 is higher still, consistent with this approach yielding an upper limit to the thermochemistry. The bond lengths determined here, 1.600 (B3LYP and BP86), 1.596 (BHLYP), and 1.591 Å (QCISD(T) and CCSD(T,full)), are in excellent agreement with the value from Ohanessian et al. of 1.605 Å.[55]

Properties of the calculated excited states of OsH^+ are discussed fully in our previous work.[54]

Os^+–C

Using Equation (7) along with the thresholds in Table 1, and $D_0(CD_2–D_2)+D_0(C–D_2)=(8.20\pm0.01)$ eV and $D_0(CH_2–H_2)+D_0(C–H_2)=(8.06\pm0.01)$ eV, BDEs for Os^+–C of (6.26 ± 0.15) and (6.15 ± 0.15) eV are obtained, in good agreement with one another. Our best experimental value for $D_0(Os^+–C)$ is the weighted average of these two values, (6.20 ± 0.21) eV, for which the uncertainty is two standard deviations of the mean. Because formation of OsC^+ is a high-energy process in this reaction system, its threshold could be shifted to higher energies because of competition with lower-energy reactions, although because it is a subsequent step, that is, decomposition of the primary $OsCD_2^+$ ion, it is not competing directly with any other process. Nevertheless, the BDE is most conservatively viewed as a lower limit to the true thermodynamic value.

Our theoretical calculations find the GS of OsC^+ to be $^4\Sigma^-$ with Os–C bond lengths of 1.684 (B3LYP), 1.670 (BHLYP), 1.695 (BP86), 1.702 (QCISD(T)), and 1.687 Å (CCSD(T,full)). The $^4\Sigma^-$ GS of OsC^+ has a valence electronic configuration of $1\sigma^2 1\pi^4 1\delta^2 2\sigma^1$, in which the 1σ orbital is a bonding combination of the $2p_z$(C) and $5d_{z2}$(Os) orbitals (z is the symmetry axis), the 2σ orbital is a nonbonding 6s–$5d_{z2}$ hybrid (largely a torus surrounding the bonding axis), the 1π orbitals are the expected $2p_{x,y}$(C)–$5d_{xz,yz}$(Os) bonding molecular orbitals, and the 1δ are pure metal $5d_{xy,x2-y2}$(Os) orbitals. There is also an excited $^2\Delta$ state lying only 0.08–0.18 eV higher in energy that has a $1\sigma^2 1\pi^4 1\delta^3$ configuration, with bond lengths of 1.635 (B3LYP), 1.617 (BHLYP), 1.646 (BP86), 1.651 (QCISD(T)), and 1.667 Å (CCSD(T,full)). Complicating the assignment of the true GS is the fact that the $^4\Sigma^-$ has no first-order spin–orbit interactions whereas the estimated spin–orbit correction for the $^2\Delta$ state lowers the energy of the $\Omega=5/2$ level by 0.38 eV. At all levels of theory, this correction makes $^2\Delta_{5/2}$ the GS. We find that the experimental bond energy is in reasonable agreement with the B3LYP, QCISD(T), and CCSD(T,full) calculations for the $^4\Sigma^-$ state before spin–orbit corrections, 5.9–6.0 eV, but not after, whereas the spin–orbit-corrected values for the $^2\Delta_{5/2}$ state ($\approx$5.9 eV) remain in reasonable agreement with the experimental value. BHLYP values are consistently much too low compared with experiment, whereas the BP86 values are high.

Other excited states of OsC^+ are $^2\Sigma^-$ ($1\sigma^2 1\pi^4 1\delta^2 2\sigma^1$), $^4\Delta$ ($1\sigma^1 1\pi^4 1\delta^3 2\sigma^1$), $^4\Pi$ ($1\sigma^2 1\pi^4 1\delta^2 2\sigma^1 2\pi^{*1}$), $^6\Pi$ ($1\sigma^1 1\pi^4 1\delta^2 2\sigma^1 2\pi^{*1}$), and $^6\Delta$ ($1\sigma^2 1\pi^3 1\delta^2 2\sigma^1 2\pi^{*1}$), in which $2\pi^*$ is an antibonding orbital. These states lie 0.71, 1.57, 2.73, 2.89, and 3.27 eV higher in energy, respectively, at the B3LYP level of theory (Table S1).

Os^+–CH

This ion is formed by dehydrogenation of the primary $OsCH_3^+$ product. The BDE of the Os^+–CH bond is determined to be (6.47 ± 0.24) eV from the CH_4 system and $D_0(Os^+–CD)=(6.84\pm0.08)$ eV from the CD_4 system (Table 2). The weighted average of these two values is (6.77 ± 0.15) eV after a zero-point energy correction of 0.037 eV for the deuterated value, for which the uncertainty is two standard deviations of the mean. We do not believe that competition with other channels is an important factor for this process because it is a subsequent step, that is, decomposition of one of the primary ions (see below). However, the bond energy is most conservatively viewed as a lower limit to the true thermodynamic value.

Irikura and Goddard estimate a value of 6.2 eV for the Os^+–CH bond by estimating an intrinsic bond strength and correcting for promotion and exchange energies.[42] Our calculated value (Table 2) of 6.45 eV (B3LYP/def2-TZVPP) is comparable to the experimental value. Here, the spin–orbit corrections do not greatly change the calculated bond energies because the estimated correction for $OsCH^+$ (0.38 eV) is nearly the same as for Os^+ (^{6}D) (0.36 eV), such that the spin–orbit-corrected bond energies increase by only 0.015 eV. BDEs calculated at the QCISD(T) and CCSD(T,full) levels are comparable to the B3LYP value, whereas BHLYP is much too low and BP86 is high compared with experiment.

Our calculations find a $^3\Delta$ GS with a geometry having r(Os–C)=1.677 and r(C–H)=1.089 Å (Figure 2 and Table S2). Thus a triple bond is clearly formed, as verified by the valence orbital occupation, ($1\sigma^2 1\pi^4 1\delta^3 2\sigma^1$), in which the CH bonding orbital is excluded for simplicity and the orbitals are comparable to those described above for OsC^+. The lowest-lying excited state is $^3\Sigma^-$, which lies 0.32 eV higher in energy and has a ($1\sigma^2 1\pi^4 1\delta^2 2\sigma^2$) configuration (Table S1). Other excited singlet states are $^1\Delta$, $^1\Sigma^+$, and $^1\Gamma$ ($1\sigma^2 1\pi^4 1\delta^3 2\sigma^1$, $1\sigma^2 1\pi^4 1\delta^4$, and $1\sigma^2 1\pi^4 1\delta^2 2\sigma^2$) lying 0.62, 1.16, and 1.38 eV higher in energy, respectively. All these states have similar Os and CH bond lengths of approximately 1.67 and 1.09 Å. A ^{5}A″ excited state is also identified lying 1.37 eV higher than the triplet GS. This state has a valence orbital occupation (given in terms of the equivalent $C_{\infty v}$ symmetry designations) of ($1\sigma^2 1\pi^4 1\delta^2 2\sigma^1 2\pi^{*1}$), but here, occupation of the π^* orbital is needed to give the high spin and this forces the geometry to bend, $\sphericalangle$OsCH=139°, and elongates the Os–C bond to 1.782 Å (Table S2). We also found a linear $^5\Pi$ state but this has an imaginary frequency of 824 cm^{-1} leading to the bent ^{5}A″ state.

We also examined the $HOsC^+$ geometry for this molecule, and found that the lowest-energy state is ^{3}A″ lying 1.03 eV above the GS $OsCH^+$ molecule. This structure has a geometry of r(OsC)=1.684 Å, indicative of a triple bond, r(OsH)=1.642 Å, and HOsC=92°. Additional states for this geometry can be found in Tables S1 and S2.

Os^+–CH_2

Reaction (3) and its perprotio analogue are exothermic, which indicates that $D_0(Os^+–CH_2)>4.71$ eV and $D_0(Os^+–CD_2)>$

4.82 eV, as previously concluded by Irikura and Beauchamp.[40] Irikura and Goddard previously used a GVB approach to calculate that $OsCH_2^+$ has a carbene (or methylidene) structure (C_{2v} symmetry) with a $^4A_2$ GS and $D_e = 4.25$ eV.[42] These authors also included an empirical correction (based largely on the experimental observations of Irikura and Beauchamp), which led to their final recommended 0 K bond energy of (4.90 ± 0.13) eV. Excited states $^6A_2$, $^2A_2$, and $^2B_2$ were found lying 1.00, 1.31, and 1.47 eV higher in energy, respectively. They also considered alternate geometries by doing explicit calculations for $TaCH_2^+$, $HTaCH^+$, and H_2TaC^+, and concluded that the alternative structures are higher in energy for all third-row metals. Using a B3LYP approach, ZLJ[45] also calculated a methylene quartet GS for $OsCH_2^+$, but did not report the symmetry (although their geometry is consistent with C_{2v}). Doublet and sextet excited states were found to lie 0.29 and 1.18 eV higher in energy, respectively. Although insufficient information is provided to reliably calculate a bond energy for $OsCH_2^+$, these authors report an overall exothermicity for the CH_4 analogue of reaction (3) as 0.18 eV at 0 K, consistent with a bond energy near 4.9 eV. Finally, Zhang and Schwarz found that $OsCH_2^+$ ($^4B_1$) had a BDE of 4.70 and 4.55 eV at the B3LYP and CCSD(T) levels, respectively, using the def2-QZVP basis set,[57] similar to the values calculated here at comparable theory levels (Table 2).

The present B3LYP/def2-TZVPP calculations find a $^4B_1$ GS for $OsCH_2^+$ with a geometry of r(Os–C) = 1.827 Å, r(C–H) = 1.093 Å, and ∢OsCH = 121.1° (Figure 2 and Table S2), comparable to that calculated by ZLJ[45] of 1.817 Å, 1.097 Å, and 121.6°, and the same as Zhang and Schwarz, 1.827 Å and 121.0°.[57] Our geometry for the low-lying $^4A_2$ state, 1.858 Å, 1.093 Å, and 122.2°, agrees better with that from Irikura and Goddard of 1.896 Å, 1.083 Å, and 122.4°. The $^4B_1$ GS of $OsCH_2^+$ has a valence electronic configuration of $(1a_1)^2(1b_1)^2(1b_2)^1(1a_2)^1(2a_1)^2(3a_1)^1$, in which the $1a_1$ and $1b_1$ orbitals are bonding, the $1b_2$, $1a_2$, and $2a_1$ orbitals are 5d nonbonding orbitals on Os (the in-plane d_π and two d_δ orbitals, respectively), and the $3a_1$ orbital is a nonbonding 6s–5dσ hybrid orbital on Os. Thus there is a covalent double bond between Os^+ and CH_2. There are several low-lying quartet excited states, $^4B_2$, $^4A_2$, and $^4B_1$, lying only 0.0004, 0.03, and 0.29 eV higher in energy, respectively, which differ only in the $(1b_2)(1a_2)(2a_1)(3a_1)$ nonbonding orbital occupation: 1211, 2111, and 1112, respectively. The near degeneracy of the $^4B_1$ and $^4B_2$ states is consistent with them differing only in which d_δ orbital is occupied. Details for other excited states can be found in Tables S1 and S2, but the lowest-lying doublet and sextet states found lie at 0.45 and 1.32 eV, $^2B_2$ and $^6A'$ ($^6A_1$), with valence electronic configurations of $(1a_1)^2(1b_1)^2(1b_2)^1(1a_2)^2(2a_1)^2$ and $(1a_1)^2(1b_1)^2(1b_2)^1(1a_2)^1(2a_1)^1(3a_1)^1(2b_1)^1$ (using the analogous C_{2v} symmetry designations), respectively, in which $2b_1$ is an antibonding π orbital. This sextet state distorts from C_{2v} symmetry by puckering such that the ∢OsCHH dihedral angle is 153°, a result of the occupied antibonding orbital. The excitation energy of the sextet state is comparable to those previously determined, whereas the doublet excitation energy agrees with ZLJ but not Irikura and Goddard. This is probably because the low-lying doublet states are all spin contaminated in the present study, thus indicating appreciable quartet state character. The lowest-energy doublet state ($^2A_1$ with a 2021 nonbonding configuration) that is not spin contaminated lies 1.65 eV above the $^4B_1$ GS, thereby agreeing better with the Irikura and Goddard result.

Calculated bond energies for the $^4B_1$ GS of $OsCH_2^+$ range from 3.97 (BHLYP) to 5.31 eV (BP86), whereas spin–orbit corrections lower the BDEs to 3.61–4.95 eV (Table 2). Notably, after spin–orbit corrections, only the BP86 result exceeds the experimental lower limit of 4.71 eV, and even before spin–orbit corrections, the QCISD(T) and CCSD(T,full) BDEs are lower than this value by 0.26 eV. Thus, formation of the osmium methylene cation may not be consistent with the experimental results. However, in contrast to previous theoretical studies, which did not explicitly explore alternate geometries, we find that the lowest-energy $[Os,C,2H]^+$ species has the $HOsCH^+$ geometry, with spin–orbit-corrected BDEs of 4.8–4.9 eV at the B3LYP, QCISD(T), and CCSD(T,full) levels of theory, for which again the BHLYP results are low (3.6 eV) and BP86 results are high (5.8 eV). Thus, the present calculations strongly suggest that the dehydrogenation of methane by Os^+ produces the hydrido carbyne osmium cation, rather than the methylene as has been previously assumed. This conclusion is further strengthened if the speculative 0.6 eV exothermicity for this reaction is assumed, as this indicates the Os^+–CH_2 bond energy approaches 5.3 eV.

The $HOsCH^+$ species is a planar molecule with a $^2A'$ GS, lying 0.52 eV below the $OsCH_2^+$ ($^4B_1$) species at the B3LYP level (Figure 2 and Tables 2 and S1). This species has a configuration that forms a covalent triple Os≡CH bond (1.672 Å) with a nearly linear ∢OsCH bond angle and a covalent single Os–H bond (1.585 Å) with a ∢HOsC bond angle of 88° consistent with σ bond formation using d orbitals. Three nonbonding electrons are located in what are essentially the two $5d_\delta$ orbitals on Os. A low-lying $^2A''$ (0.35 eV higher in energy) simply moves one of these electrons between these two $5d_\delta$ orbitals, which results in a very similar geometry. There are also $^4A''$, $^4A'$, and ^6A states of $HOsCH^+$ lying 1.26, 1.87, and 3.66 eV above the $^2A'$ GS (Tables S1 and S2). The quartet states promote one of the $5d_\delta$ electrons to a π* antibonding orbital (either in the plane of the molecule or perpendicular to it, respectively), thus leading to longer OsC bond lengths of 1.733 and 1.767 Å, respectively, and for the $^4A''$ state, an ∢OsCH bond angle of 154°. The sextet state occupies both π* antibonding orbitals after promoting a bonding π electron, which leads to distortion to nonplanarity, ∢HOsCH = 101°, and ∢OsCH = 141°.

Os^+–CH_3

A reliable cross section for $OsCH_3^+$ could not be obtained because of mass overlap with the much more intense $OsCH_2^+$ product. $OsCD_3^+$ could be resolved but has a very small cross section resulting from competition with OsD^+ and decomposition to $OsCD^+ + D_2$. Hence, the results listed in Table 1 were obtained by analyzing the sum of the $OsCD_3^+$ and $OsCD^+$ product cross sections. This leads to a BDE for Os^+–CD_3 of (2.87 ± 0.15) eV, a value that is less reliable because of the small size of the $OsCD_3^+$ cross section. Corrections for zero-point energy differences depend on the geometry assumed for

the $OsCH_3^+$ species, but are less than 0.02 eV in all cases, such that we simply assign our value of (2.87 ± 0.15) eV as the BDE of Os^+–CH_3. Notably, the threshold determined for formation of $OsCD_3^+$ lies well below that for OsD^+, by (0.57 ± 0.16) eV. As noted above, because there is competition with the dehydrogenation reaction, the BDE of OsH^+ determined from methane systems is too small and a similar result seems likely for $OsCH_3^+$. However, we can use the shift determined for OsH^+ ((0.13 ± 0.12) eV) to give our best estimate of the Os^+–CH_3 bond energy as (3.00 ± 0.19) eV. This is equivalent to measuring that the threshold for $OsCD_3^+$ lies 0.57 eV below that for OsD^+, such that once zero-point effects are included, the Os^+–CH_3 bond strength exceeds that for Os^+–H by (0.55 ± 0.16) eV.

As mentioned above, Holthausen et al.[43] carefully considered the most appropriate choice of level of theory for the first- and third-row transition-metal methyl cations. B3LYP, BHLYP, and QCISD(T) levels of theory gave predicted Os^+–CH_3 bond energies (D_e) of 3.33, 2.82, and 2.53 eV, respectively. On the basis of results for the first-row metal methyl cations compared with experimental values, empirical corrections of −0.22 and +0.16 eV were applied to their BHLYP and QCISD(T) results leading to final estimated bond energies of 2.60 and 2.69 eV with estimated errors of ±0.22 eV. These values are below our adjusted experimental value of (3.00 ± 0.17) eV as well as the uncorrected value ((2.87 ± 0.15) eV).

The present B3LYP/def2-TZVPP calculations locate the GS of $OsCH_3^+$ as ^5E with C_{3v} symmetry (Figure 2), consistent with previous work.[43] The Os–C and C–H bond lengths (2.015 and 1.095 Å) and OsCH bond angles (107.4°) calculated here (B3LYP, Table S2) are comparable to those from Holthausen et al. (2.013 and 1.100 Å and 107.7°, B3LYP; 2.023 and 1.089 Å, and 107.8°, BHLYP; 2.034 and 1.096 Å and 108.3°, QCISD(T)). We also find a low-lying $^5A_1$ state with an excitation energy of 0.31 eV, in which a $5d_\delta$ electron is promoted to the nonbonding sd_σ hybrid orbital. A series of triplet and singlet excited states lying 0.74–1.90 eV above the GS, all of which have C_s symmetry, were also located as detailed in Tables S1 and S2.

Our B3LYP calculations obtain a D_0 value of 3.00 eV for the osmium methyl cation (Table 2), in good agreement with our adjusted experimental value, and spin–orbit corrections reduce this by only 0.17 eV such that reasonable agreement is maintained. BDEs calculated at the QCISD(T) and CCSD(T,full) levels are about 0.15 eV lower, such that the spin–orbit corrections drop them below our experimental value. These calculations also indicate that the Os^+–CH_3 bond is slightly stronger than the Os^+–H bond but only by 0.08 eV according to B3LYP, QCISD(T), and CCSD(T,full) levels. These calculated differences are inconsistent with the measured difference of (0.55 ± 0.16) eV, which suggests that the $[Os,C,3H]^+$ species formed experimentally may not have a simple osmium-methyl structure.

Alternative structures for the $[Os,C,3H]^+$ species include $HOsCH_2^+$, $HOsHCH^+$, and $(H_2)OsCH^+$ (Figure 2). The lowest in energy of all $[Os,C,3H]^+$ species is the dihydride carbyne, $HOsHCH^+$, which has a $^1A'$ GS lying 0.68 eV below $OsCH_3^+$ (^5E). Likewise the hydrido methylene, $HOsCH_2^+$, with a $^3A''$ GS, is also more stable than the methyl structure, but only by 0.07 eV. The dihydrogen carbyne complex, $(H_2)OsCH^+$, is the highest-energy species lying 1.52 eV above $HOsHCH^+$ ($^1A'$). Excited states of each of these species are included in Tables S1 and S2. Evidence for the presence of the $HOsHCH^+$ species is the large difference in the thresholds for formation of OsH^+ and $[Os,C,3H]^+$, (0.55 ± 0.16) eV, which matches that calculated: 0.76 eV (0.59 eV with spin–orbit corrections) at the B3LYP level (QCISD(T) and CCSD(T,full) differences are closer to 1 eV; see Table 2). However, the agreement between the experimental BDEs of (3.00 ± 0.19) eV is still slightly better if compared to the spin–orbit-corrected BDEs calculated for $OsCH_3^+$ (which are low) versus those for $HOsHCH^+$ (which are high) at the B3LYP, QCISD(T), and CCSD(T,full) levels (Table 2). One possible explanation is that both species can be formed experimentally such that the measured threshold describes a weighted average of both species. The small size of the cross section does not allow this possibility to be explored more fully.

Potential energy surfaces of $[Os,C,4H]^+$

We constructed the potential energy surfaces for interaction of Os^+ with methane at the B3LYP/def2-TZVPP level of theory and included zero-point energy corrections (scaled by 0.989). In most cases, we located transition states by using relaxed potential energy surface scans along reasonable reaction pathways, followed by geometry optimization and frequency calculations to locate the transition states and intrinsic reaction coordinate calculations to confirm that the transition states connect the affiliated initial and final intermediates. In some cases, we also used the synchronous transit-guided quasi-Newton method (QST3).[58,59] As discussed above, the B3LYP level of theory reproduces the bond energies of Os^+–CH_x species adequately. Thus the relative characteristics of these surfaces are likely to be qualitatively correct, and are of the most interest here. Table 3 provides a summary of the theoretical energies for the lowest-energy intermediates and transition states of each spin state, with structures shown in Figures S2–S4. Table S3 contains energy information about these and additional states and Table S4 lists detailed structural information for all these species.

The discussion of our results is broken down into several parts. Results for formation of the osmium methylene cation product, $OsCH_2^+$, parallel those previously outlined by ZLJ,[45] whose results are included in Tables 3 and S4, although these authors never specify the symmetry of any of their species and do not explore several alternative pathways described here. Our potential energy surfaces for this path are presented in Figure 3a. Shown in Figure 3b are the potential energy surfaces associated with the formation of $HOsCH^+$, the hydrido carbyne cation. As noted above, this is the lowest-energy $[Os,C,2H]^+$ species rather than the metal methylene cation. In past theoretical studies of MCH_2^+ species, such alternative structures have largely been ignored, although it was proposed by Maître and co-workers for W^+,[60] and it has been explored in the $Ir^+ + CH_4$ reaction, in which spectroscopic evidence for $HIrCH^+$ was found.[46]

Table 3. B3LYP/def2-TZVPP theoretical energies of $[Os,C,4H]^+$ intermediates and transition states.

Species	State	$s(s+1)$[a]	Energy [E_h]	ZPE [E_h][b]	E_{rel} [eV][c]	ZLJ [eV][d]
$Os^+ + CH_4$	$^6D + {}^1A_1$	8.75	−130.822601	0.044113	0.000	0.00
	$^4F + {}^1A_1$	*4.46	−130.794813	0.044113	0.756	0.89
	$^2G + {}^1A_1$	*2.44	−130.774875	0.044113	1.299	2.21
$Os^+(CH_4)$ (**1**)	$^4A''$	3.76	−130.844616	0.041018 (68i)	−0.696	–
	$^4A'$	3.76	−130.837776	0.042474	−0.458	–
	^6A	8.75	−130.837185	0.043864	−0.404	−0.57
	$^2A''$	*1.74	−130.822469	0.041801	−0.059	–
TS1/5	$^4A'$	3.78	−130.786019	0.038265 (874i)	0.836	–
	^2A	*1.75	−130.768174	0.038115 (905i)	1.318	–
	$^6A'$	8.77	−130.744932	0.031481 (1355i)	1.770	–
CP1($^6A'$–$^4A''$)	$^6A'$	8.77	−130.832418	–	−0.450	−0.35
CP1($^6A'$–$^4A'$)	$^6A'$	8.77	−130.803469	–	−0.327	–
CP1($^4A''$–$^6A'$)	$^4A''$	3.85	−130.826538	–	−0.214	–
CP1($^4A'$–$^6A'$)	$^4A'$	3.85	−130.827394	–	−0.149	–
CP1($^6A'$–$^2A''$)	$^6A'$	8.77	−130.818339	–	−0.062	0.02
CP1(^2A–^6A)	^2A	1.74	−130.809625	–	0.082	–
CP1($^6A'$–$^2A'$)	$^6A'$	8.77	−130.805841	–	0.280	–
TS1/2	$^4A'$	3.76	−130.837098	0.040077 (641i)	−0.504	–
	^2A	1.76	−130.822329	0.040855 (179i)	−0.071	–
	$^6A'$	8.75	−130.766884	0.037141 (685i)	1.326	0.97
$HOsCH_3^+$ (**2**)	$^4A''$	3.77	−130.873486	0.039579 (47i)	−1.508	−1.79
	$^4A'$	3.77	−130.866847	0.040378	−1.306	–
	$^2A''$	*1.75	−130.851359	0.039392	−0.911	−1.19
	$^6A'$	8.75	−130.815235	0.038898	0.059	−0.25
TS2/3	^2A	*1.30	−130.845321	0.038169 (698i)	−0.780	−1.09
	^4A	3.77	−130.822110	0.035023 (846i)	−0.234	−0.66
=CP2(^4A–^2A)	^4A	3.77	−130.822110	0.035023 (846i)	−0.234	−0.57
TS2/3	^6A	8.77	−130.743305	0.033440 (503i)	1.867	1.50
CP3(^2A–^4A)	^2A	–	−130.846234	–	−0.803	−1.07
CP5(^4A–^2A)	^4A	3.76	−130.829963	–	−0.454	–
CP6(^4A–^2A)	^4A	3.76	−130.831246	–	−0.489	–
TS2/4	^4A	3.76	−130.812385	0.034709 (838i)	0.022	–
	^6A	8.77	−130.743072	0.032697 (408i)	1.853	–
$HOsHCH_2^+$ (**3**)	^2A	0.77	−130.876251	0.037233	−1.647	−2.03
	$^4A''$	3.76	−130.834261	0.035687	−0.547	−1.02
	$^6A_1$	8.75	−130.764259	0.035073	1.342	0.92
CP4(^2A–^4A)	^2A	0.77	−130.829523	–	−0.381	−0.71
TS3/4	^4A	3.77	−130.820306	0.033422 (514i)	−0.228	−0.68
	^2A	*1.68	−130.813274	0.036979 (151i)	0.060	−0.25
	$^6A'$	8.76	−130.761183	0.033834 (265i)	1.392	0.99
$(H_2)OsCH_2^+$ (**4**)	$^4A_2$	3.82	−130.835228	0.038041	−0.509	–
	$^4A''$	3.77	−130.833874	0.036610	−0.511	-0.87
	^2A	*1.67	−130.813856	0.037970	0.071	–
	$^2B_1$	*1.76	−130.805659	0.035411	0.224	−0.24
	$^6A_1$	8.76	−130.780506	0.034828 (65i)	0.893	–
	$^6A'$	8.76	−130.780526	0.035054	0.898	0.58
$OsCH_2^+ + H_2$ (**5**)	$^4B_1 + {}^1\Sigma_g^+$	–	−130.813652	0.033027	−0.058	−0.18
	$^2B_2 + {}^1\Sigma_g^+$	–	−130.796077	0.031873	0.389	0.11
	$^6A' + {}^1\Sigma_g^+$	–	−130.762562	0.030416	1.261	0.99
TS3/6	^2A	0.75	−130.829434	0.033730 (999i)	−0.468	–
	^4A	3.77	−130.745751	0.033270 (629i)	1.796	–
	^6A	8.76	−130.684635	0.030228 (490i)	3.376	–
TS3/7	^4A	3.76	−130.767702	0.030599 (1284i)	1.126	–
H_3OsCH^+ (**6**)	$^2A''$	0.75	−130.850188	0.035372	−0.989	–
	$^2A'$	0.75	−130.844690	0.035177	−0.844	–
	$^4A'$	3.77	−130.764723	0.031675	1.236	–
	$^6A'$	8.75	−130.704116	0.030727	2.860	–
TS6/7	^2A	0.75	−130.845238	0.033148 (758i)	−0.914	–
	^4A	3.77	−130.764212	0.030852 (511i)	1.228	–
	^6A	8.76	−130.704089	0.030224 (299i)	2.847	–
$(H_2)HOsCH^+$ (**7**)	$^2A'$	0.76	−130.854565	0.036011	−1.090	–
	$^4A''$	3.77	−130.799536	0.033355	0.335	–
	^6A	8.76	−130.714990	0.036759	2.728	–
$HOsCH^+ + H_2$ (**8**)	$^2A' + {}^1\Sigma_g^+$	–	−130.830016	0.030173	−0.581	–
	$^4A'' + {}^1\Sigma_g^+$	–	−130.781471	0.028001	0.681	–
	$^6A + {}^1\Sigma_g^+$	–	−130.692091	0.026752	3.079	–

Sextet surface: $OsCH_2^+$ formation

Interaction of Os^+ (^6D, $6s^15d^6$) with methane leads initially to the formation of an $Os^+(CH_4)$ (**1**) adduct in which the methane molecule remains intact and largely unperturbed. The methane binds in an η^3 conformation in a ^6A state, which nearly has C_{3v} symmetry but the geometry would not converge under this symmetry constraint (Figure S2). This adduct lies 0.40 eV below the reactant asymptote. Upon further reduction of the Os–H bond length, the system passes over a transition state, ^{6}TS1/2, which leads to the insertion intermediate H–Os^+–CH_3 (**2**). This transition state has C_s symmetry ($^6A'$) and an H–Os–C bond angle of 67.0° (Figure S2). The energy of this transition state is quite high, 1.33 eV, which indicates that oxidative addition of the CH bond to Os^+ (^6D) is not a viable pathway for the dehydrogenation reaction (3). The $HOsCH_3^+$ intermediate retains the $^6A'$ state (C_s symmetry) and has an H–Os–C bond angle of 142.2° (Figure S2). In this molecule, both the Os–H and Os–C distances, 1.695 and 2.099 Å, respectively, are about 0.09 Å longer than those of OsH^+ ($^5\Pi$), 1.600 Å, and $OsCH_3^+$ (^5E), 2.015 Å. This observation along with the Os–C–H bond angles of approximately 108° indicate that the methyl group is covalently bound to Os in this state. The HOs^+–CH_3 bond energy is calculated to be 1.18 eV. A $^6A''$ state of $HOsCH_3^+$ was also located 0.50 eV higher in energy and has a nearly linear HOsC arrangement with a much longer Os–C bond length of 2.370 Å.

Continuing along the sextet surface, the $HOsHCH_2^+$ dihydride methylene intermediate

Table 3. (Continued)

Species	State	$s(s+1)$[a]	Energy [E_h]	ZPE [E_h][b]	E_{rel} [eV][c]	ZLJ [eV][d]
$OsH^+ + CH_3$	$^5\Pi + {}^2A^{+\prime\prime}$	–	−130.757311	0.034299	1.510	–
$HOsHCH^+ + H$	$^1A' + {}^2S$	–	−130.780573	0.029231	0.739	–
$OsCH_3^+ + H$	$^5E + {}^2S$	–	−130.760282	0.033821	1.416	–
$OsC^+ + 2H_2$	$^4\Sigma^- + {}^1\Sigma_g^+$	–	−130.726219	0.022244	2.028	–
$OsCH^+ + H_2 + H$	$^3\Delta + {}^1\Sigma_g^+ + {}^2S$	–	−130.706616	0.022903	2.579	–

[a] Values indicating spin contamination are marked with an asterisk. [b] Zero-point energies scaled by 0.989. Imaginary frequencies [cm^{-1}] in parentheses. [c] Energy relative to the ground-state reactants including zero-point energies scaled by 0.989. [d] Values from Zhang, Li, and Jiang.[45]

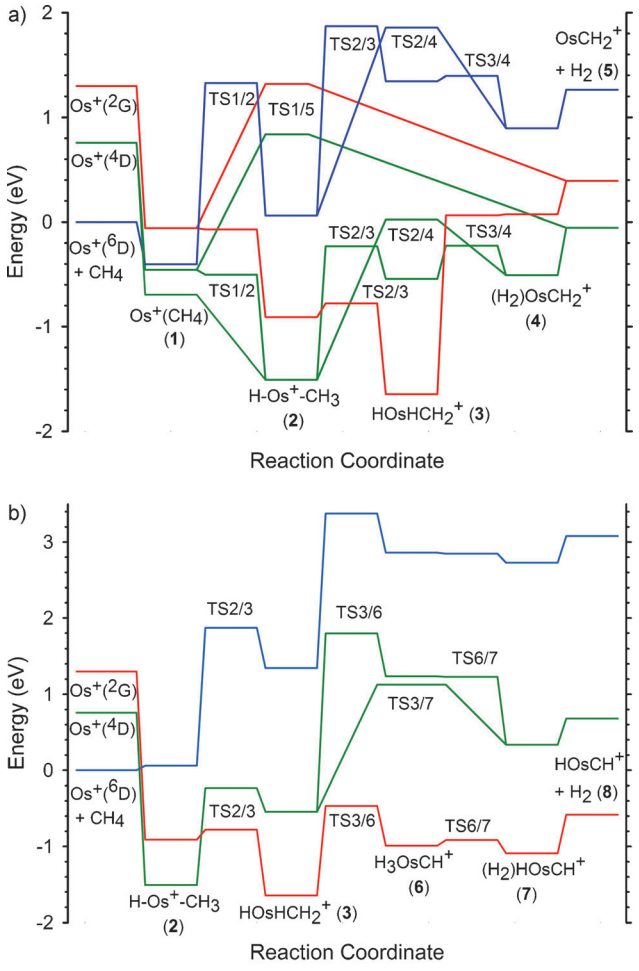

Figure 3. $[Os,C,4H]^+$ potential energy surfaces at 0 K derived from theoretical results for formation of the $OsCH_2^+$ (a) and $HOsCH^+$ (b) product ions for sextet (blue), quartet (green), and doublet (red) spin states. Labels for the minima refer to all three spin surfaces. The relative energies of all species are based on quantum chemical calculations (B3LYP/def2-TZVPP, Table 3). Energies are relative to the Os^+ (^6D) + CH_4 ground-state asymptote. TS = transition state.

(**3**) is reached via ^{6}TS2/3 (Figure 3a), which lies 1.87 eV above GS reactants and 1.81 eV above the $HOsCH_3^+$ intermediate. This $^6A_1$ intermediate lies 1.34 eV above the reactants and has Os–H (1.649 Å) and Os–C (2.029 Å) distances indicating covalent bonding interactions as they are similar to those of OsH^+ (1.600 Å) and $OsCH_3^+$ (2.015 Å). Clearly Os cannot form a double bond with CH_2 in this species to maintain the high spin state. The dihydride methylene intermediate converts to the $(H_2)OsCH_2^+$ intermediate (**4**) via ^{6}TS3/4, which lies only 0.05 eV higher than the dihydride. The $(H_2)OsCH_2^+$ intermediate has C_s symmetry with an H_2 bond length of 0.791 Å, slightly extended compared to that of free H_2 (0.743 Å). The dihydrogen is tilted slightly to one side of this molecule distorting the geometry of the $OsCH_2^+$ part of the molecule. If C_{2v} symmetry is imposed on the entire molecule, a $^6A_1$ transition state in which the H_2 ligand rocks to the other side is found, with an imaginary frequency of 65 cm^{-1}. Interestingly, once zero-point energies are accounted for, the transition state actually lies 0.005 eV lower in energy. From this intermediate, loss of H_2 is facile as the H_2–$OsCH_2^+$ bond energy is calculated to be only 0.36 eV relative to the $OsCH_2^+$ ($^6A'$) + H_2 asymptote.

An alternative pathway for transition between the $HOsCH_3^+$ and $(H_2)OsCH_2^+$ intermediates was also located and involves the four-centered transition state ^{6}TS2/4, a pathway not explored by ZLJ. This transition state lies 1.79 eV above $HOsCH_3^+$ ($^6A'$) and 1.85 eV above the ground-state reactants. The limiting transition state for the sequential α-H migration pathway (^{6}TS2/3) is slightly higher in energy (by 0.014 eV) than the four-centered pathway of ^{6}TS2/4 (Figure 3a). We also explored whether the $Os^+(CH_4)$ intermediate could eliminate H_2 directly (as found for the lower spin states), but no such transition state could be located on the sextet surface.

Quartet surface: $OsCH_2^+$ formation

The interaction of methane with the quartet state of Os^+ (^4F, $5d^7$) leads initially to the formation of an $Os^+(CH_4)$ adduct (**1**) in which the methane molecule distorts severely as the C–H bond begins to break (Figure S3). We located both $^4A''$ and $^4A'$ species with similar geometries, although the former also had an imaginary frequency (68 cm^{-1}) that led directly to the inserted $HOsCH_3^+$ intermediate. Neither of these species was located by ZLJ.[45] These intermediates were calculated to lie 0.70 and 0.46 eV below the Os^+ (^6D) + CH_4 reactants. Upon further reduction of the Os–H bond length, the $^4A'$ species passes over a transition state, ^{4}TS1/2 ($^4A'$) with an HOsC bond angle of 41°, which leads to the insertion intermediate H–Os^+–CH_3. Once zero-point energies are included, the energy of ^{4}TS1/2 is lower than that of the $Os^+(CH_4)$ ($^4A'$) intermediate by 0.05 eV, and along the $^4A''$ surface, the $Os^+(CH_4)$ intermediate already has an imaginary frequency. Thus, oxidative addition of the C–H bond of methane to Os^+ (^4F) is spontaneous, as previously concluded by ZLJ.[45]

The quartet $HOsCH_3^+$ intermediate (**2**) lies below the comparable species having sextet and doublet spin, as would be expected according to Hund's rules for a species forming two covalent bonds, thus leaving five electrons in four nonbonding orbitals. Both $^4A'$ and $^4A''$ intermediates have C_s symmetry and

HOsCH dihedral angles of ±60 and 180°, and lie 1.51 and 1.31 eV, respectively, below the GS reactants. Oddly, the ^{4}A″ intermediate had an imaginary frequency of 47 cm^{-1} corresponding to a methyl rotation. Potential energy scans of this motion locate a minimum at ∢HOsCH = 177.4° but optimizations from this geometry revert to the C_s symmetry species and imaginary frequency. In the ^{4}A′ species, rotation of the methyl group to HOsCH dihedral angles of 0 and ±120° leads to another stable ^{4}A′ state lying 0.04 eV higher in energy. The analogous species along the ^{4}A″ surface is a transition state. The $HOsCH_3^+$ quartet intermediate found by ZLJ appears most similar to our ^{4}A″ state (Tables 3 and S4) and was found to lie 1.79 eV below the reactants.

From either state of $HOsCH_3^+$, an $HOsHCH_2^+$ (^{4}A″) dihydride methylene intermediate (**3**) is reached via ^{4}TS2/3 (Figure 3a). This transition state has no symmetry (Figure S3) and lies 1.27 eV above $HOsCH_3^+$ (^{4}A″) and 0.31 eV higher in energy than $HOsHCH_2^+$ (^{4}A″). The two Os–H (1.644 Å) and Os–C (1.820 Å) bond lengths of $HOsHCH_2^+$ are slightly longer than those of OsH^+ ($^5\Pi$; 1.600 Å) and comparable to $OsCH_2^+$ ($^4B_1$; 1.827 Å), thus indicating the formation of covalent bonds. The quartet dihydride methylene is calculated to lie 0.55 eV below the GS reactants, somewhat less stable than the results of ZLJ at 1.02 eV; however, both studies place the quartet species approximately 1.0 eV above the more stable doublet dihydride methylene.

The quartet $HOsHCH_2^+$ intermediate can eliminate dihydrogen by passing over ^{4}TS3/4, which lies only 0.32 eV higher in energy (0.34 eV, ZLJ). The ground $(H_2)OsCH_2^+$ (^{4}A″) intermediate has an H_2 bond length of 0.848 Å compared to free H_2 at 0.743 Å. It lies 0.51 eV (0.87 eV, ZLJ) below the GS reactants. In addition, we find several states of $(H_2)OsCH_2^+$ that are planar and have C_{2v} symmetry: $^4A_2$, $^4B_1$, and $^4B_2$, which lie 0.002, 0.137, and 0.138 eV higher in energy, respectively (Table S3). Before zero-point energy corrections, the $^4A_2$ is actually lower in energy than the bent ^{4}A″ state, but the H_2 vibrational frequency is substantially higher in the former state (3500 versus 2982 cm^{-1}), consistent with the much shorter H_2 bond in these species: 0.803, 0.763, and 0.763 Å, respectively. The $(H_2)OsCH_2^+$ intermediates can then dissociate to H_2 and $OsCH_2^+$ ($^4B_1$), the GS methylene products, which lie 0.06 eV below the GS reactants. ZLJ find an exothermicity for this reaction of 0.18 eV. These values can be compared favorably with the experimental exothermicity observed for this reaction, but spin–orbit corrections (estimated below) of 0.36 eV change these values to 0.30 and 0.18 eV endothermic.

Although elimination of H_2 from $HOsCH_3^+$ via the dihydride is the lowest-energy pathway, two alternative pathways were also explored (neither of which was characterized by ZLJ). First, $HOsCH_3^+$ can reductively eliminate H_2 directly over ^{4}TS2/4, which lies 0.25 eV above ^{4}TS3/4 (which is only 0.00$_6$ eV above ^{4}TS2/3). It is also possible for the initial $Os^+(CH_4)$ adduct to lose H_2 directly, as originally elucidated for dehydrogenation of methane by Au^+.[33] Here, ^{4}TS1/5 is substantially higher in energy than the other pathways, lying 0.84 eV above GS reactants (Figure 3a).

Doublet surface: $OsCH_2^+$ formation

The interaction of methane with the doublet state of Os^+ (^{2}G, 5d^7) leads initially to the formation of an $Os^+(CH_4)$ adduct in which the methane molecule is strongly distorted as the C–H bond is activated (Figure S4). Several states, ^{2}A″, $^2B_1$, ^{2}A′, and $^2B_2$, were located (all of which were spin contaminated) and lie 0.64, 0.82, 1.04, and 1.33 eV above $Os^+(CH_4)$ (^{4}A″) (Table S3). As for the quartet surface, ZLJ located none of these intermediates. Upon further reduction of the Os–H bond length, the system passes over a transition state, ^{2}TS1/2, which has an HOsC bond angle of 36° and leads to the insertion intermediate H–Os^+–CH_3 (^{2}A″) (**2**). As for the analogous quartet species, once zero-point energies are included, the energy of ^{2}TS1/2 is lower than $Os^+(CH_4)$ (Figure 3a), which indicates that C–H bond activation is spontaneous. We calculate that ^{2}TS1/2 and $HOsCH_3^+$ (^{2}A″) lie 0.07 and 0.91 eV (1.19 eV, ZLJ), respectively, below the GS reactants. We also located a ^{2}A′ state of this intermediate lying 0.29 eV higher in energy.

Continuing along the doublet surface, the system passes over ^{2}TS2/3 to form the global minimum of all potential energy surfaces, the $HOsHCH_2^+$ (^{2}A) dihydride methylene osmium cation (**3**), which lies 1.65 eV (2.03 eV, ZLJ) below the GS reactants (Figure S4). The ^{2}TS2/3 lies 0.87 eV (0.94 eV, ZLJ) higher in energy than the $HOsHCH_2^+$ (^{2}A) intermediate and 0.13 eV (0.10 eV, ZLJ) above the $HOsCH_3^+$ (^{2}A″) intermediate. A doublet spin state is anticipated for a molecule with four covalent bonds to Os^+, which leaves three electrons divided between two nonbonding orbitals. Indeed, Os–H (1.578 and 1.585 Å) and Os–C (1.806 Å) distances in this intermediate indicate covalent bonding interactions as they are similar to those of OsH^+ ($^5\Pi$) (1.600 Å) and $OsCH_2^+$ ($^4B_1$) (1.827 Å). In our work, several attempts were made to locate a four-centered ^{2}TS2/4 transition state, but these always collapsed directly to a transition state leading to the dihydride intermediate.

From the dihydride intermediate, the reaction can proceed on the doublet surface to eliminate H_2. This ^{2}TS3/4 transition state between $HOsHCH_2^+$ (^{2}A) and $(H_2)OsCH_2^+$ (^{2}A) lies 0.06 eV above the GS reactants (0.25 eV below, ZLJ). We identified several $(H_2)OsCH_2^+$ intermediate states, but the lowest of these actually lies 0.01 eV above ^{2}TS3/4 once zero-point energies are included. Thus, the dihydrogen osmium methylene cation complex inserts spontaneously to form the dihydride methylene (**3**) on the doublet surface. The $^2A_2$, $^2B_1$, $^2A_1$, and $^2B_2$ excited states of $(H_2)OsCH_2^+$ lie 0.11, 0.22, 1.11, and 1.35 eV above the GS reactants (Table S3). These are all planar structures with H_2 bond lengths of 0.764–0.805 Å compared to free H_2 at 0.743 Å (Table S4). The $^2A_2$ state has an imaginary frequency of 306 cm^{-1} corresponding to an out-of-plane bend that leads to the ^{2}A GS. The lower-lying $^2A_2$ and $^2B_1$ states are spin contaminated, $s(s+1) = 1.7$, with structures similar to those of the $^4A_2$ and $^4B_1$ states of this species. In the studies of ZLJ, the $(H_2)OsCH_2^+$ (^{2}A) intermediate appears to have a geometry most similar to our $^2B_1$ state, although theirs does not have C_{2v} symmetry. They found it to lie 0.24 eV below GS reactants and 1.79 eV above the $HOsHCH_2^+$ global minimum, compared with 0.22 above and 1.87 eV from our calculations.

Viewed more globally, we find our potential energy surface (Figure 3a) is qualitatively consistent in many respects with the previously reported potential energy surfaces of ZLJ,[45] with comparable intermediates and transition states along the pathways examined by ZLJ. As noted above, these authors did not examine alternative pathways, that is, TS2/4 and TS1/5, although these are higher-energy pathways for all spin surfaces except the sextet. A more detailed comparison shows that the results of ZLJ are quantitatively similar to the present results, with energetic differences of (0.3±0.1) eV for 24 different intermediates, transition states, and products along the doublet, quartet, and sextet surfaces. The present calculations appear to have been more successful in characterizing the $Os^+(CH_4)$ adducts on the low-spin surfaces than the approach of ZLJ.

Crossing points between surfaces of different spin

Examination of Figure 3a shows that formation of ground-state $OsCH_2^+$ ($^4B_1$) + H_2 ($^1\Sigma_g^+$) products from ground-state reactants requires changing the spin from sextet to quartet. The efficiency of this spin change is influenced by the extent of spin–orbit coupling (enhanced by the presence of the heavy metal) as well as the character of the seam over which the two spin surfaces interact. To approximate the character of the crossing seams, we take the approach of Yoshizawa et al.[61] Thus, an intrinsic reaction coordinate scan or relaxed potential energy surface scan along a likely region of coordinate space for each spin state is conducted at the B3LYP/def2-TZVPP level of theory, and then the energies of the other spin states at the same geometries are calculated at the same level of theory. In general, this can lead to two crossing points between the surfaces for which a complex of a specific geometry has the same energy in both spin states, with a crossing seam between these points. ZLJ[45] used the same approach to find many of the crossing points discussed herein. Structures at all crossing points can be found in the Supporting Information, Figure S5.

In the entrance channel, the potential energy surfaces are shown in Figure 4, with crossing points indicated by circles. We find seven crossing points in this region (CP1), three of which occur as the osmium cation approaches methane (open circles). Along the optimized quartet surfaces (both $^4A''$ and $^4A'$) and the $^2A''$ surface, there are crossings with the sextet surface at −0.21, −0.15, and 0.08 eV, respectively, relative to the GS reactants. Four crossing points (solid circles) happen along the optimized sextet surface between the $Os^+(CH_4)$ (^6A) intermediate and ^{6}TS1/2. The sextet surface crosses those of the $^4A''$, $^4A'$, $^2A''$, and $^2A'$ surfaces at energies of −0.45, −0.33, −0.06, and 0.28 eV, respectively, compared to the GS reactants. ZLJ located the two crossing points (called SI_{6-4} and SI_{6-2}) between the ^6A and the lower $^4A''$ and $^2A''$ surfaces at energies they calculate are approximately 0.1 eV higher than found here. Note that these crossing energies are in the same vicinity as the speculative modeling of the $OsCD_2^+$ cross section above 0.1 eV, which suggested a surface crossing energy E_c near −0.25 eV.

Although there are no crossing seams between the doublet and quartet states in the entrance channel, they do occur in

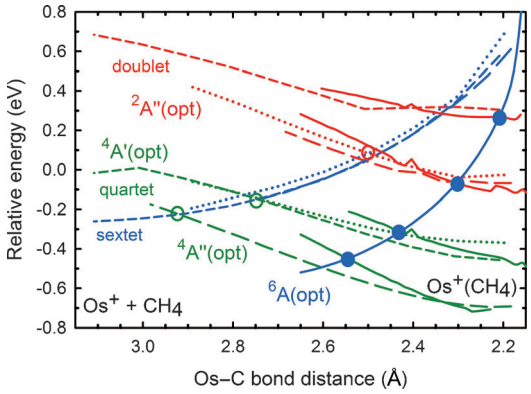

Figure 4. Potential energy surfaces and crossing points (CP1) from reactants to $Os^+(CH_4)$ complex (**1**) along the optimized (opt) quartet (green dashed lines and open circles) and doublet surfaces (red dotted lines and open circle) and from the $Os^+(CH_4)$ complex (**1**) to TS1/2 along the optimized sextet surface (blue solid lines and solid circles). Zero-point energies are not included.

the region of TS2/3 and TS3/4, as detailed by Figures S6 and S7. We find that CP2 lies exactly at ^{4}TS2/3, 0.23 eV below the GS reactants, whereas ZLJ find this crossing point (called SII_{4-2}) slightly below the transition state. CP3 lies very close to ^{2}TS2/3 (0.02 eV below), in agreement with the findings of ZLJ ($SIII_{4-2}$). Another crossing point is found along the doublet surface as the $HOsHCH_2^+$ (**3**) intermediate evolves towards $(H_2)OsCH_2^+$ (**4**). We find CP4 to lie 0.38 eV below the GS reactants, whereas ZLJ find SIV_{4-2} to be at −0.71 eV. In agreement with ZLJ, no crossing point is found along the optimized quartet surface (Figure S7). We also located crossing points in the vicinity of ^{4}TS2/4 (a pathway not explored by ZLJ). As shown in Figure 5, CP5 is found between $HOsCH_3^+$ (**2**) and TS2/4 at 0.45 eV below GS reactants, whereas CP6 is between TS2/4 and $(H_2)OsCH_2^+$ (**4**) at 0.49 eV below GS reactants. Note that CP5 and CP6 could allow the system to form $(H_2)OsCH_2^+$ ($^4A''$) directly from $HOsCH_3^+$ ($^4A'$) at lower energies than ^{4}TS2/4, as transferring to the doublet surface has a rate-limiting transition state that is 0.28 eV below ^{4}TS2/4. This makes it 0.03 eV below ^{4}TS2/3; however, the minimum along the doublet (nonoptimized) surface in Figure 5 corresponds to a geometry similar

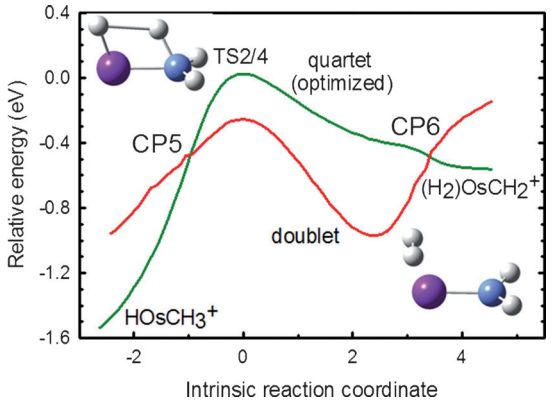

Figure 5. Potential energy surfaces and crossing points (CP5 and CP6, structures shown) from the $HOsCH_3^+$ (**2**) intermediate to $(H_2)OsCH_2^+$ (**4**) along the optimized quartet surface. Zero-point energies are not included.

to $HOsHCH_2^+$, such that this species would probably collapse to this low-energy intermediate.

$HOsCH^+$ formation

Figure 3b shows the potential energy surfaces calculated for dehydrogenation of methane by Os^+ to form the $HOsCH^+$ product ion, with structures for the lowest-energy pathway shown in Figure 6. Figure 3b simplifies the pathways for formation of the dihydride osmium methylene cations, $HOsHCH_2^+$ (**3**), from those shown in more detail in Figure 3a. From the doublet state of **3**, another α-H transfer over ^{2}TS3/6 at 0.47 eV below reactants forms the trihydride osmium carbyne cation, H_3OsCH^+ (**6**). This species has both a $^2A''$ and $^2A'$ state lying 0.99 and 0.84 eV, respectively, below GS reactants. In the lower $^2A''$ state, the Os–C bond is 1.686 Å long with an OsCH bond angle of 179.8°, which are comparable to the characteristics of $OsCH^+$ ($^3\Delta$), 1.677 Å and 180°, indicating a triple bond. The three Os–H bond lengths are 1.575 and 1.633 (2) Å, the latter being slightly longer than the 1.600 Å bond of OsH^+ ($^5\Pi$). In contrast, the three Os–H bonds in the $^2A'$ state are 1.585(2) and 1.617 Å, with the Os–C bond 1.724 Å and ∢OsCH = 155.1°. Now, the Os–C bond is in between that of $OsCH^+$ ($^3\Delta$) and $OsCH_2^+$ ($^4B_1$) (1.827 Å), which suggests a bond order more like 2.5.

From the lower $^2A''$ state, only 0.08 eV is needed to surpass ^{2}TS6/7 and form $(H_2)HOsCH^+$ (**7**), a dihydrogen adduct of the final product ion. Two forms of this species were located, one of which has C_s symmetry in which the center of the H_2 molecule lies in the $HOsCH^+$ plane (Figure 6) and another in which the H_2 molecule lies perpendicular to this plane. The former lies 1.09 eV below the GS reactants and the latter is 0.15 eV higher in energy. From the former, it takes 0.51 eV to remove the H_2 to yield $HOsCH^+$ ($^2A'$). Note that ^{2}TS3/6 lies slightly higher in energy than the product asymptote but still well below the energy of $OsCH_2^+ + H_2$ (Table 3).

A parallel pathway is found along the quartet surface. The ^{4}TS3/6 transition state is again rate limiting and lies 1.80 eV above the GS reactants and 1.12 eV above the $HOsCH^+$ ($^4A''$) + H_2 product asymptote. The quartet H_3OsCH^+ (**6**) intermediate lies 0.01 eV above the energy of ^{4}TS6/7 once zero-point energies are included, such that this species collapses to $(H_2)HOsCH^+$ ($^4A''$), 0.34 eV above GS reactants. Only 0.35 eV is needed to remove the H_2 molecule to form the $HOsCH^+$ ($^4A''$) product. Because of the instability of the H_3OsCH^+ species on the quartet surface, it is also possible to directly convert $HOsHCH_2^+$ to $(H_2)HOsCH^+$ via ^{4}TS3/7. This transition state lies 1.13 eV above the GS reactants and 0.67 eV below ^{4}TS3/6, such that it is the lowest-energy pathway for forming $HOsCH^+$ ($^4A''$). TS3/7 was also looked for on the doublet surface but always collapsed to ^{2}TS3/6. This is consistent with the fact that an estimated energy for ^{2}TS3/7 (obtained by using the geometry of ^{4}TS3/7) is 0.30 eV above ^{2}TS3/6.

Along the sextet surface, the energies of these various species all lie near 3 eV above the GS reactants (Figure 3b). Again, H_3OsCH^+ collapses to $(H_2)HOsCH^+$ and ^{6}TS3/6 is the rate-limiting step.

Note that Figure 3b indicates that there are no crossings between surfaces of different spin as $HOsHCH_2^+$ evolves to form $HOsCH^+ + H_2$. Thus, once $HOsHCH_2^+$ (^2A) is formed, it can evolve to GS $HOsCH^+$ ($^2A'$) + H_2 products with no spin changes required.

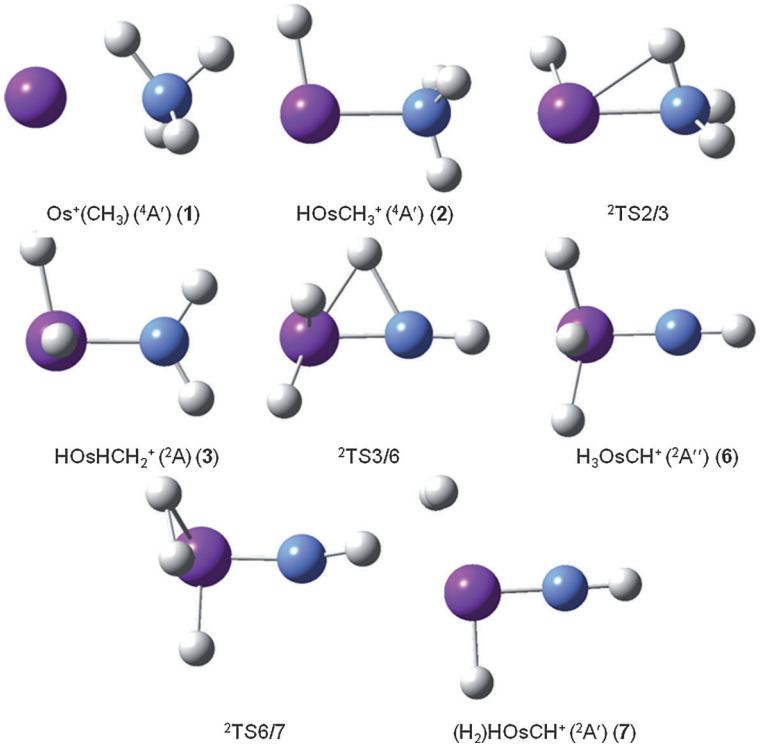

Figure 6. Structures of several intermediates and transition states along the lowest-energy adiabatic surface of the $[Os,C,4H]^+$ system for formation of $HOsCH^+ + H_2$ calculated at the B3LYP/def2-TZVPP level of theory.

Discussion

The σ-bond activation by atomic metal ions is generally explained by using a simple donor–acceptor (oxidative addition) model in which an empty orbital on the metal ion accepts electrons donated from the bond to be broken. Concomitantly, metal electrons in orbitals having π symmetry back-donate into the antibonding orbital of the bond to be broken. An occupied acceptor orbital leads to repulsive interactions and inefficient reaction either by more direct abstraction pathways or by introduction of a barrier to the reaction. In our previous studies,[16–22] the activation of methane by atomic metal ions was explained by this simple donor–acceptor model in which oxidative addition of a C–H bond to M^+ forms an $H–M^+–CH_3$ intermediate. For the reaction of Os^+ with methane, the calculated potential energy surfaces, both those determined here and those of ZLJ, confirm this process and explain why the reaction along the sextet surface (on which all metal orbitals must be occupied) is so much more repulsive than the lower spin surfaces. Because Os^+ (^{6}D, $6s^15d^6$) has no empty va-

lence orbitals, the simple donor–acceptor process is restricted, thus leading to the high barrier for ^{6}TS1/2. The energies of ^{6}TS2/3, ^{6}TS3/4, and ^{6}TS2/4 are even higher because the high spin does not allow formation of the several covalent bonds needed to stabilize these three transition states.

Mechanism for dehydrogenation of Os^+ with methane to form $OsCH_2^+$

Because of the high energy of the sextet surface, at low collision energies, reaction of Os^+ (^{6}D) with methane must occur by coupling to the quartet surface at which oxidative addition of CH_4 to Os^+ produces a quartet hydrido methyl osmium cation intermediate, H–Os^+–CH_3 (^{4}A′,^{4}A″). On the quartet surface, the empty s orbital of Os^+(^{4}F, 5d^7) acts as an efficient acceptor orbital, and a doubly occupied 5dπ orbital can provide an efficient donor orbital. This leads naturally to an intermediate in which Os^+ forms two covalent bonds using 6s5d hybrids.

From H–Os^+–CH_3 (^{4}A′,^{4}A″), the activation of a second C–H bond (α-H transfer) can lead to formation of a dihydride methylene osmium cation intermediate, $HOsHCH_2^+$ (^{4}A″). Reductive elimination of dihydrogen then forms the $(H_2)OsCH_2^+$ (^{4}A″) intermediate that easily loses dihydrogen to form the GS $OsCH_2^+$ ($^4B_1$)+H_2 products. Note that ^{4}TS1/2, ^{4}TS2/3, and ^{4}TS3/4 all lie below the energy of the $OsCH_2^+$ ($^4B_1$)+H_2 products, such that the dehydrogenation reaction is barrierless along the quartet surface (although not after estimated spin–orbit corrections). This is similar to the mechanism found for the dehydrogenation reactions of methane with Pt^+ (^{2}D), although here the reaction remains on a doublet surface throughout.[27,62–64] This pathway differs from those of the first-row transition-metal ions, which are equivalent to the four-centered transition state, TS2/4, that bypasses the dihydride intermediate. Along the quartet surface, this pathway lies at higher energies than the dihydride pathway but is only 0.02 eV above the GS reactants.

However, the global minimum on the potential energy surface is $HOsHCH_2^+$ (^{2}A). Thus, dehydrogenation may also occur by coupling between the quartet and doublet surfaces. Once the H–Os^+–CH_3 (^{4}A′,^{4}A″) intermediate is formed, it can cross over to the doublet surface at the seam between CP2 (or CP5) and CP3 forming the $HOsHCH_2^+$ (^{2}A) intermediate. Reductive 1,1-elimination of dihydrogen on the doublet surface must then couple back to the quartet surface to form $(H_2)OsCH_2^+$ (^{4}A″), followed by loss of dihydrogen to yield $OsCH_2^+$ ($^4B_1$)+H_2 with an overall reaction energy of −0.06 eV (0.30 eV including spin–orbit corrections) at the B3LYP/def2-TZVPP level and 0.24 (0.60) eV at the CCSD(T,full)/def2-TZVPP level. This type of mechanism is also available for W^+ (^{6}D), Re^+ (^{7}S), and Ir^+ (^{5}F) reacting with methane, for which multiple spin changes are also required.[28,32,34] Overall, ZLJ concluded that this mechanism was operative.

Mechanism for dehydrogenation of Os^+ with methane to form $HOsCH^+$

As noted above, theory is divided about whether formation of the osmium methylene cation, $OsCH_2^+$, is exothermic; however, our theoretical results show that a lower-energy rearrangement transforms the $HOsHCH_2^+$ (^{2}A) global minimum into the trihydride carbyne, H_3OsCH^+ (^{2}A″,^{2}A′). Reductive 1,1-elimination of dihydrogen from this intermediate leads to formation of $(H_2)HOsCH^+$ (^{2}A″,^{2}A), followed by loss of dihydrogen to yield $HOsCH^+$ (^{2}A′)+H_2 with an overall reaction energy of −0.58 eV (−0.22 eV including spin–orbit corrections) at the B3LYP/def2-TZVPP level and −0.50 (−0.14) eV at the CCSD(T,full)/def2-TZVPP level. This overall pathway lies 0.52 eV (0.74 eV at the CCSD(T,full) level) below that forming the methylene structure. This type of mechanism has been demonstrated to be low in energy for Ir^+ (^{6}D) reacting with methane, for which infrared action spectroscopy has demonstrated that the $HIrCH^+$ structure is the dominant species formed by dehydrogenation of methane by Ir^+.[46] For other third-row transition-metal cations, this same study demonstrates that dehydrogenation of methane by Ta^+, W^+, and Pt^+ all form a methylene structure, albeit with agostic distortions for the two early metals. Formation of the hydrido carbyne structure cannot be ruled out in the tungsten system and is conceivable in the Re^+ system, in which the dehydrogenation reaction is no longer exothermic.[28] Importantly, the formation of the more stable $HMCH^+$ isomer requires sufficient electrons to form four covalent bonds (which also forces a low-spin state), such that this process is not expected for early (before Ta^+) and late (after Ir^+) metal cations.

Mechanism for higher-energy products

As the energy available increases above about 1.5 eV, OsH^+ and $OsCH_3^+$ products can be formed by simple bond cleavages from the H–Os^+–CH_3 intermediate. These processes, in particular formation of OsH^++CH_3, deplete the population of this first stable intermediate formed such that the cross section for the dehydrogenation process declines commensurately. Because dehydrogenation is thermodynamically preferred by >2 eV (Table 2), this competition indicates that formation of OsH^++CH_3 must be preferred kinetically. This is consistent with a simple bond cleavage of HOs^+–CH_3 at elevated kinetic energies, whereas the elimination of H_2 occurs through the more restricted pathways discussed above. Kinetically, formation of $OsCH_3^+$ is most favorable from the parallel pathway in which it is formed by simple bond cleavage of H_3COs^+–H at elevated kinetic energies. The thermodynamically preferred $HOsHCH^+$ structure can also be formed by simple bond cleavages from the doublet $HOsHCH_2^+$ and H_3OsCH^+ intermediates; however, because formation of these intermediates is more complicated than that for the initially formed $HOsCH_3^+$ species, it is feasible that formation of this lower-energy isomer is kinetically restricted. This could explain the experimental observation that the onset for formation of $[Os,C,3H]^+$ falls in between the calculated thermochemistry for $OsCH_3^+$ and $HOsHCH^+$.

At higher energies, OsC^+ and $OsCH^+$ products are formed by dehydrogenation of the primary products, $OsCH_2^+$ and $OsCH_3^+$, respectively. The thermochemistry determined above (Table 2) shows that these dehydrogenations require >(1.86±0.21) and (0.82±0.24) eV, respectively. Comparable observations have been made for second-row[18,23,24,65,66] and third-row (W^+, Re^+, Ir^+, and Pt^+) metal systems.[27,28,32,34]

Conclusion

Ground-state Os^+ ions are found to be highly reactive with methane over a wide range of kinetic energies. At low energies, dehydrogenation is efficient, exothermic, and the only primary process observed. At high energies, the dominant process is formation of $OsH^+ + CH_3$. This channel is favored over the $OsCH_3^+ + H$ channel because of angular momentum constraints, even though $OsCH_3^+ + H$ is measured to have a threshold over 0.5 eV lower in energy. At higher energies, the $OsCH_2^+$ and $OsCH_3^+$ products decompose by dehydrogenation to form OsC^+ and $OsCH^+$, respectively. Analyses of the kinetic energy dependences of the reaction cross sections provide the bond dissociation energies (BDEs) of Os^+–CH_3, Os^+–CH, and Os^+–C. The exothermicity of reaction (3) establishes that the BDE for Os^+–CH_2 is >4.71 eV. These experimental bond energies are stronger than the corresponding ones of the first-row and second-row transition-metal congeners, Fe^+ and Ru^+,[7,19,21,66–70] which can be attributed to the accessibility of the s^1d^6 electronic configuration and effective sd hybridization, a consequence of relativistic effects. Our experimental BDEs are found to be in reasonable agreement with quantum chemical calculations performed here and in the literature (Table 2).

Calculations are also used to provide a detailed potential energy surface for the $OsCH_4^+$ system. As found previously,[45] this potential energy surface shows that the reaction of Os^+ (^{6}D) with methane proceeds through the oxidative addition of one C–H bond to yield a hydrido-methyl osmium intermediate, H–Os^+–CH_3 (^{4}A′,^{4}A″). OsH^+ and $OsCH_3^+$ can be formed by simple bond cleavages from this intermediate. The activation of a second C–H bond proceeds through a three-centered transition state involving migration of an H atom from C to Os^+ to form an $HOsHCH_2^+$ (^{2}A or ^{4}A″) intermediate, for which $HOsHCH_2^+$ (^{2}A) is the global minimum. This intermediate can also evolve to H_3OsCH^+ (^{2}A″) or dissociate at high energies to form $HOsHCH^+$, an isomer of $OsCH_3^+$. The $HOsHCH^+$ species is lower in energy than $OsCH_3^+$ but its formation requires a more convoluted path, such that both species can conceivably be formed. Reductive elimination of H_2 from the $HOsHCH_2^+$ (^{2}A or ^{4}A″) or H_3OsCH^+ (^{2}A″) intermediates can form the electrostatic complexes $(H_2)OsCH_2^+$ (^{4}A″) and $(H_2)HOsCH^+$ (^{2}A′), from which H_2 is eliminated to form the metal methylene complex $OsCH_2^+$ ($^4B_1$) + H_2, or hydrido carbyne complex $HOsCH^+$ (^{2}A′) + H_2, the latter being much lower in energy. OsC^+ and $OsCH^+$ are formed by the dehydrogenation of the $HOsCH^+$ (or $OsCH_2^+$) and $OsCH_3^+$ (or $HOsHCH^+$) primary products, respectively.

Overall, dehydrogenation of methane by Os^+ may have three available pathways. One pathway requires only a single spin change: Os^+ (^{6}D) + CH_4 ($^1A_1$)→H–Os^+–CH_3 (^{4}A′,^{4}A″)→$HOsHCH_2^+$ (^{4}A″)→$(H_2)OsCH_2^+$ (^{4}A″)→$OsCH_2^+$ ($^4B_1$) + H_2 ($^1\Sigma_g^+$). Another pathway requires three spin changes: Os^+ (^{6}D) + CH_4 ($^1A_1$)→H–Os^+–CH_3 (^{4}A′,^{4}A″)→$HOsHCH_2^+$ (^{2}A)→$(H_2)OsCH_2^+$ (^{4}A″)→$OsCH_2^+$ ($^4B_1$) + H_2 ($^1\Sigma_g^+$). These mechanisms agree with those previously proposed by ZLJ,[45] but the present levels of theory suggest that these reactions are slightly endothermic. This theory also indicates that a clearly exothermic pathway and the lowest-energy adiabatic pathway for dehydrogenation involves two spin changes and the formation of the $HOsCH^+$ species: Os^+ (^{6}D) + CH_4 ($^1A_1$)→H–Os^+–CH_3 (^{4}A′,^{4}A″)→$HOsHCH_2^+$ (^{2}A)→H_3OsCH^+ (^{2}A″)→$(H_2)HOsCH^+$ (^{2}A′)→$HOsCH^+$ (^{2}A′) + H_2 ($^1\Sigma_g^+$). Despite the need to change spin, the dehydrogenation reaction is found to occur with high efficiency (near 100%) at the lowest energies, thus suggesting that spin conservation is not an impediment for reaction of this heavy-metal system. This conclusion is similar to that drawn for the $Re^+ + CH_4$ system, for which the reaction efficiency is (86 ± 10)% even though three spin changes must occur for dehydrogenation,[28] and to the $Ir^+ + CH_4$ system, for which spin must change from quintet to singlet (perhaps through a triplet) and yet the reaction occurs with 100% efficiency.[32,46] Interestingly, there is some evidence that spin conservation may play a role at higher collision energies, as the experimental cross section for dehydrogenation cannot be modeled quantitatively without including a Landau–Zener probability for switching between adiabatic states.

Experimental Section

Instrumentation

The guided-ion-beam tandem mass spectrometer on which these experiments were performed has been described in detail previously.[71] Briefly, reactant ions are generated in a direct-current discharge flow tube source described below.[72] The ions are extracted from the source, accelerated, and focused into a magnetic sector momentum analyzer for mass selection of the primary reactant ions. Mass-selected ions are decelerated to a desired kinetic energy and focused into an octopole ion-beam guide, which uses radio-frequency (rf) electric fields to trap the ions in the radial direction and ensure complete collection of reactant and product ions.[73,74] The octopole passes through a static gas cell that contains the reaction partner at a low pressure (usually ≤0.3 mTorr) so that multiple ion–molecule collisions are improbable. With one clear exception, all products reported herein resulted from single bimolecular encounters, as verified by pressure dependence studies. Product and unreacted primary ions drift to the end of the octopole where they are extracted, focused, passed through a quadrupole mass filter for mass analysis, and subsequently detected with a secondary electron scintillation ion detector using standard pulse-counting techniques. Ion intensities were converted to absolute cross sections after correcting for background signals.[48] Absolute uncertainties in cross-section magnitudes were estimated to be ±20% and relative uncertainties were ±5%.

The kinetic energy dependence of the ions was varied in the laboratory frame by scanning the dc bias on the octopole with respect to the potential of the ion source region. Ion kinetic energies in the laboratory frame, E_{lab}, were converted to energies in the center-of-mass frame, E_{CM}, by using the formula $E_{CM} = E_{lab}m/(m+M)$, in which m and M are the neutral and ionic reactant masses, respectively. All energies reported below are in the CM frame unless otherwise noted. Two effects broadened the cross-section data: the thermal motion of the neutral reactant gas (Doppler broadening) and the kinetic energy distribution of the reactant ion.[75,76] The absolute zero and distribution of the ion kinetic energies were determined by using the octopole beam guide as a retarding potential analyzer as described previously.[48] The distribution of ion kinetic energies was nearly Gaussian and had a typical full width at

half maximum of 1.0–1.4 eV (lab) in these studies. The uncertainties in the absolute energy scale were ±0.05 eV (lab).

Ion source

Atomic osmium metal cations were formed in a direct-current discharge flow tube source.[72] This source consisted of a cathode held at high negative voltage (1.2–1.6 kV) over which a flow of approximately 90% He and 10% Ar passed at a total pressure of 0.3–0.5 Torr and ambient temperature. The cathode in this work was an osmium/vanadium alloy disk attached to an iron holder. Ar^+ ions created in the discharge were accelerated toward the metal cathode, thereby sputtering Os^+ ions. These ions were then swept down a 1 m long flow tube. The flow conditions used in this ion source provided about 10^5 thermalizing collisions between an ion and He ($\approx 10^4$ collisions with Ar) before the ions entered the guided-ion-beam apparatus. Generally, these conditions have been found to thermalize the ions, thereby producing atomic ions in their ground electronic state. No evidence for low-lying excited states of the metal ions (such as cross-section features having lower energy thresholds) within about 1% sensitivity was observed under these flow conditions in this work or previous work on reactions of Os^+ with H_2, HD, and D_2.[54] On the basis of comparisons to a surface ionization source, the direct-current discharge flow tube source has been found to generate Sc^+,[77] Fe^+,[78] Co^+,[79] Ni^+,[80] Ru^+,[70] Rh^+,[70] and Pd^+[70] ions with an average electronic temperature of (700±400) K, and Y^+, Zr^+, Nb^+, and Mo^+ ions with an average electronic temperature of (300±100) K.[81] The populations of Os^+ ions created under such conditions have been discussed in a previous paper,[54] and rely on energies taken from spectroscopic work in the literature.[82,83] Most Os^+ ions are in the ground electronic term, ^6D ($6s^15d^6$), and largely in the lowest spin–orbit level ($J=9/2$) even at the highest likely temperature (98.9%). The estimated populations are consistent with the failure to observe any evidence for electronically excited Os^+ species in the present and past studies and lead to a negligible uncertainty (<0.01 eV) in the electronic energy of the Os^+ reactant.

Data analysis

The kinetic energy dependence of product cross sections was analyzed to determine E_0, the energy threshold for product formation at 0 K. E_0 differs from the apparent threshold observed under laboratory conditions because of the kinetic and internal energy distributions of the reactants. These contributions allow reactions to occur at energies below E_0. To determine E_0, endothermic reaction cross sections were modeled by using Equation (8):[53,84,85]

$$\sigma(E) = \sigma_0 \Sigma g_i (E + E_i + E_{el} - E_0)^n / E \quad (8)$$

in which σ_0 is an energy-independent scaling factor, E is the relative kinetic energy of the reactants, and n is an adjustable parameter. There is an explicit sum of contributions from rovibrational states of reactants at 300 K, denoted by i, which have energies E_i and populations g_i, with $\Sigma g_i = 1$. The various sets of vibrational frequencies and rotational constants used to determine E_i in this work were taken from the literature for CH_4[86] and CD_4.[86] As noted above, E_{el} at (700±400) K is believed to be <0.01 eV for Os^+ and thus is negligible. Before comparison with the experimental data, Equation (8) was convoluted with the kinetic energy distributions of the ions and neutral reactants at 300 K.[48] The σ_0, n, and E_0 parameters were then optimized using a nonlinear least-squares analysis to give the best reproduction of the data. Error limits for E_0 were calculated from the range of threshold values for different data sets over a range of acceptable n values combined with the absolute uncertainty in the kinetic energy scale and electronic energy.

Theoretical calculations

In general, quantum chemistry calculations reported herein utilized the B3LYP hybrid density functional method[87,88] and were performed with the Gaussian 09 suite of programs.[89] The B3LYP functional was used because it provides reasonable results for the analogous Hf^+, Ta^+, W^+, Re^+, Ir^+, and Pt^+ with CH_4 systems.[27–30,32,34] In all cases, the thermochemistry reported herein was corrected for zero-point energy effects using frequencies scaled by 0.989. The basis set used for osmium, carbon, and hydrogen was def2-TZVPP, a balanced basis set of triple-ζ quality with polarization functions. This basis set gives good results for the thermochemistry of methane and dihydrogen, with deviations from experiment of less than 0.06 eV for the bond energy of $H–CH_3$ (4.418 vs. 4.478 eV), $H_2–CH_2$ (4.679 vs. 4.713 eV), H–CH (4.346 vs. 4.360 eV), C–H (3.525 vs. 3.465 eV), and H–H (4.510 vs. 4.478 eV). (See Table 1 of Ref. [27] for experimental thermochemistry used for all H, D, CH_x, and CD_x species.) For osmium, the def2-TZVPP basis set uses a small core (60 electron) effective core potential (ECP) developed by Andrae et al.,[90] in which the 5s, 5p, 5d, and 6s orbitals are retained in the valence space. This basis set includes f- and g-type polarization functions on Os,[91] with a contraction scheme of (8s7p6d2f1g)/[6s4p3d2f1g]. (The def2-TZVPP basis set was obtained from the Basis Set Exchange of the Environmental and Molecular Sciences Laboratory, EMSL.[92,93])

The most appropriate choice for a level of theory has been thoroughly investigated for the first- and third-row transition-metal methyl cations by Holthausen et al.[43] and for first-row transition-metal methylene cations by Holthausen, Mohr, and Koch.[94] In the first study, the authors used B3LYP, Beck-Half-and-Half-LYP (BHLYP), and QCISD(T) methods with a basis set consisting of a polarized double-zeta basis on C and H and the Hay–Wadt relativistic ECP with valence electrons added. The symmetries of the metal methyl species were constrained to C_{3v}. For the first-row MCH_3^+ species (M=Sc–Cu), for which experimental results are available for all metals,[7] these authors concluded that the B3LYP functional overbinds, with a mean absolute deviation (MAD) from experiment of 0.41 eV. The BHLYP functional and the QCISD(T) methods performed more accurately, with MADs of 0.18 and 0.20 eV, respectively. For the third-row elements, the bond energies calculated using B3LYP were again higher than those for BHLYP and QCISD(T). In contrast, for the metal methylene complexes,[94] the BHLYP functional predicted bond energies consistently below experimental values, whereas the performance of the B3LYP functional was quite good. In addition, these authors found that the results depended on the basis set used for the metal ion with an all-electron basis providing better results than ECP methods. Recent work has also shown that the BP86 functional performs well for a variety of transition-metal complexes[95] and has been found to yield reasonable upper limits on the thermochemistry of organometallic species in previous work, in which B3LYP gave reasonable lower limits.[96] This was also found in the specific case of OsO^+,[97] for which CCSD(T,full) calculations were also somewhat low. On the basis of these results, the present study includes calculations for the various product ions using the B3LYP, BHLYP, and BP86 functionals along with QCISD(T) and CCSD(T,full) calculations, all using the def2-TZVPP basis set on all elements. Such calculations will be explicitly noted, but unless otherwise designated, results refer to a B3LYP/def2-TZVPP level of theory.

One means of evaluating the level of theory and basis set used in the calculations is to compare electronic excitation energies of Os^+ with those from experiment. Experimental values for the excitation energies (average over all spin–orbit states) from the ^6D ($6s^15d^6$) GS to the ^6S ($6s^25d^5$), ^4D ($6s^15d^6$), and $^4F(5d^7)$ excited states are 0.62, 1.11, and 1.28 eV, respectively.[82,83] Note that the values for the quartet states are somewhat tenuous because all spin–orbit levels have not been identified. In previous studies of Os^+,[54,97] we have explored a range of theoretical approaches and basis sets. Among these, a CCSD(T,full)/def2-TZVPP approach yielded excitation energies in reasonable agreement with experiment (0.79, 0.92, and 0.88 eV, respectively) with an MAD below 0.26 eV, whereas B3LYP/def2-TZVPP was somewhat farther off but still reasonable (1.01, 1.18, and 0.76 eV, respectively) with a 0.33 eV MAD. Overall, the CCSD(T,full)/def2 calculations appear to yield the best performance.

Estimate of spin–orbit effects

Explicit spin–orbit calculations are beyond the scope of the present study and are not included here; however, a qualitative idea of the effect that spin–orbit interactions might have on the thermochemistry obtained here can be considered. The experimental BDEs refer to the ground spin–orbit state at 0.0 eV, $^6D_{9/2}$ for Os^+. In contrast, our calculations are referenced to the statistically weighted mean of all spin–orbit levels in the ground term, 0.36 eV for Os^+ (^6D).[82] Because our calculations do not explicitly include spin–orbit interactions, it is possible that all calculated bond energies may need to be reduced by this different asymptotic energy before comparison with experimental values. However, spin–orbit effects also influence the energetics of many of the intermediates and products. Indeed, Balasubramanian and co-workers have calculated that spin–orbit effects for OsH and OsH_2^+ can be large,[98,99] up to 0.80 eV for the highly excited $^6\Pi$ state of OsH, but are much smaller, 0.06–0.20 eV, for all other OsH states and about 0.1 eV for OsH_2^+ states.

In the present study, we estimated the spin–orbit corrections of the various product ions containing Os as follows. Our procedure starts by noting that the spin–orbit splitting of the OsN molecule, isovalent with $OsCH_2^+$, in its $^4\Phi$ state has been measured with a difference between the $^4\Phi_{7/2}$ and $^4\Phi_{5/2}$ states of 979.26 cm^{-1} = 0.12 eV.[100,101] Assuming that the spin–orbit splitting energy is given by $E^{so} = A\Lambda M_S$, in which A is the spin–orbit splitting constant, Λ is the orbital angular momentum quantum number, and M_S is the spin quantum number associated with a particular $\Omega = \Lambda + M_S$ level,[102] the measured splitting should equal three times the spin–orbit splitting constant, such that $A(^4\Phi) = 326.42$ cm^{-1}. In this case, $A(^4\Phi)$ should be approximately $\zeta_{5d}(Os)/9 \approx 3045$ $cm^{-1}/9 =$ 338 cm^{-1},[100,101] in which $\zeta_{5d}(Os)$ is the atomic spin–orbit constant, in good agreement with the experimental value. For species in the present study, we utilized this value of $\zeta_{5d}(Os)$ to estimate the spin–orbit splitting corrections, which necessarily ignores possible interactions with other states. For most species, there are no estimated spin–orbit corrections because the Λ quantum number is zero and the Os^+–L bond energies for these species can be reduced by the 0.36 eV average energy of the ^6D state of Os^+. For other species, we estimate that the $^5\Pi$ and ^5E GSs of OsH^+ and $OsCH_3^+$ have A constants of $-\zeta_{5d}(Os)/4 = -761$ cm^{-1} and that their ground levels ($\Omega = 3$) should lie $\zeta_{5d}(Os)/2 = 0.19$ eV below the unperturbed states. The $^2\Delta$ state of OsC^+ is estimated to have $A = -\zeta_{5d}(Os)$ with the $\Omega = 5/2$ ground level lying 0.38 eV below the unperturbed state. For $OsCH^+$ ($^3\Delta$), $A \approx -\zeta_{5d}(Os)/2$ leads to $\Omega = 3$ ground level lying 0.38 eV below the unperturbed state. For these four systems, the Os^+–L bond energies are increased by these stabilization energies and decreased by the 0.36 eV energy of the Os^+ (^6D) state. Clearly, this procedure may still introduce errors of several tenths of an electron volt in the calculated energetics.

Acknowledgements

This study was supported by the National Science Foundation (Grant CHE-1049580). Michael Morse is thanked for supplying the Os sample and for several very useful conversations. Dedicated to Detlef Schröder, who was a great colleague and friend.

Keywords: bond energy · C–H activation · density functional calculations · osmium · thermochemistry

[1] H. Schwarz, *Angew. Chem.* **2011**, *123*, 10276 – 10297; *Angew. Chem. Int. Ed.* **2011**, *50*, 10096 – 10115.
[2] J. Roithová, D. Schröder, *Chem. Rev.* **2010**, *110*, 1170 – 1211.
[3] J. Allison, *Prog. Inorg. Chem.* **1986**, *34*, 627 – 676.
[4] R. R. Squires, *Chem. Rev.* **1987**, *87*, 623 – 646.
[5] K. Eller, H. Schwarz, *Chem. Rev.* **1991**, *91*, 1121 – 1177.
[6] D. H. Russell, *Gas Phase Inorganic Chemistry*, Plenum, New York, **1989**.
[7] P. B. Armentrout, B. L. Kickel in *Organometallic Ion Chemistry* (Ed.: B. S. Freiser), Kluwer, Dordrecht, **1996**, pp. 1 – 45.
[8] P. B. Armentrout in *Topics in Organometallic Chemistry, Vol. 4* (Eds.: J. M. Brown, P. Hofmann), Springer-Verlag, Berlin, **1999**, pp. 1 – 45.
[9] E. Sicilia, N. Russo, *J. Am. Chem. Soc.* **2002**, *124*, 1471 – 1480.
[10] N. Russo, E. Sicilia, M. D. C. Michelini, *J. Phys. Chem. A* **2002**, *105*, 8937 – 8944.
[11] S. G. Chiodo, O. Kondakova, M. D. C. Michelini, E. Sicilia, A. Irigoras, J. Ugalde, N. Russo, *J. Phys. Chem. A* **2004**, *108*, 1069 – 1081.
[12] R. H. Crabtree, *The Organometallic Chemistry of the Transition Metals, 2nd ed.*, Wiley, New York, **1994**.
[13] G. A. Somorjai, *Introduction to Surface Chemistry and Catalysis*, Wiley, New York, **1994**.
[14] P. B. Armentrout, M. R. Sievers, *J. Phys. Chem. A* **2003**, *107*, 4396 – 4406.
[15] F. Liu, X.-G. Zhang, P. B. Armentrout, *Phys. Chem. Chem. Phys.* **2005**, *7*, 1054 – 1064.
[16] N. Aristov, P. B. Armentrout, *J. Phys. Chem.* **1987**, *91*, 6178 – 6188.
[17] L. S. Sunderlin, P. B. Armentrout, *J. Phys. Chem.* **1988**, *92*, 1209 – 1219.
[18] Y.-M. Chen, P. B. Armentrout, *J. Phys. Chem.* **1995**, *99*, 10775 – 10779.
[19] R. H. Schultz, J. L. Elkind, P. B. Armentrout, *J. Am. Chem. Soc.* **1988**, *110*, 411 – 423.
[20] R. Georgiadis, P. B. Armentrout, *J. Phys. Chem.* **1988**, *92*, 7067 – 7074.
[21] C. L. Haynes, Y.-M. Chen, P. B. Armentrout, *J. Phys. Chem.* **1995**, *99*, 9110 – 9117.
[22] C. L. Haynes, Y.-M. Chen, P. B. Armentrout, *J. Phys. Chem.* **1996**, *100*, 111 – 119.
[23] Y.-M. Chen, M. R. Sievers, P. B. Armentrout, *Int. J. Mass Spectrom. Ion Processes* **1997**, *167/168*, 195 – 212.
[24] M. R. Sievers, Y.-M. Chen, C. L. Haynes, P. B. Armentrout, *Int. J. Mass Spectrom.* **2000**, *195/196*, 149 – 170.
[25] L. S. Sunderlin, P. B. Armentrout, *J. Am. Chem. Soc.* **1989**, *111*, 3845 – 3855.
[26] P. B. Armentrout, *J. Phys. Chem. A* **2006**, *110*, 8327 – 8338.
[27] X.-G. Zhang, R. Liyanage, P. B. Armentrout, *J. Am. Chem. Soc.* **2001**, *123*, 5563 – 5575.
[28] M. M. Armentrout, F.-X. Li, P. B. Armentrout, *J. Phys. Chem. A* **2004**, *108*, 9660 – 9672.
[29] L. G. Parke, C. S. Hinton, P. B. Armentrout, *Int. J. Mass Spectrom.* **2006**, *254*, 168 – 182.
[30] L. G. Parke, C. S. Hinton, P. B. Armentrout, *J. Phys. Chem. C* **2007**, *111*, 17773 – 17787.
[31] L. G. Parke, C. S. Hinton, P. B. Armentrout, *J. Phys. Chem. A* **2008**, *112*, 10469 – 10480.
[32] F.-X. Li, X.-G. Zhang, P. B. Armentrout, *Int. J. Mass Spectrom.* **2006**, *255/256*, 279 – 300.

[33] F.-X. Li, P. B. Armentrout, *J. Chem. Phys.* **2006**, *125*, 133114.
[34] P. B. Armentrout, S. Shin, R. Liyanage, *J. Phys. Chem. A* **2006**, *110*, 1242 – 1260.
[35] P. B. Armentrout, R. V. Hodges, J. L. Beauchamp, *J. Chem. Phys.* **1977**, *66*, 4683 – 4688.
[36] H. H. Cornehl, C. Heinemann, D. Schröder, H. Schwarz, *Organometallics* **1995**, *14*, 992 – 999.
[37] J. K. Gibson, R. G. Haire, J. Marcalo, M. Santos, A. P. d. Matos, M. K. Mrozik, R. M. Pitzer, B. E. Bursten, *Organometallics* **2007**, *26*, 3947 – 3956.
[38] E. Di Santo, M. C. Michelini, N. Russo, *Organometallics* **2009**, *28*, 3716 – 3726.
[39] K. J. de Almeida, H. A. Duarte, *Organometallics* **2009**, *28*, 3203 – 3211.
[40] K. K. Irikura, J. L. Beauchamp, *J. Phys. Chem.* **1991**, *95*, 8344 – 8351.
[41] A. Shayesteh, V. V. Lavrov, G. K. Koyanagi, D. K. Bohme, *J. Phys. Chem. A* **2009**, *113*, 5602 – 5611.
[42] K. K. Irikura, W. A. Goddard III, *J. Am. Chem. Soc.* **1994**, *116*, 8733 – 8740.
[43] M. C. Holthausen, C. Heinemann, H. H. Cornehl, W. Koch, H. Schwartz, *J. Chem. Phys.* **1995**, *102*, 4931.
[44] K. K. Irikura, J. L. Beauchamp, *J. Am. Chem. Soc.* **1991**, *113*, 2769 – 2770.
[45] G. Zhang, S. Li, Y. Jiang, *Organometallics* **2003**, *22*, 3820 – 3830.
[46] V. J. F. Lapoutre, B. Redlich, A. F. G. van der Meer, J. Oomens, J. M. Bakker, A. Sweeney, A. Mookherjee, P. B. Armentrout, *J. Phys Chem. A*, **2013**, *117*, 4115 – 4126.
[47] G. Gioumousis, D. P. Stevenson, *J. Chem. Phys.* **1958**, *29*, 294 – 299.
[48] K. M. Ervin, P. B. Armentrout, *J. Chem. Phys.* **1985**, *83*, 166 – 189.
[49] K. K. Irikura, J. L. Beauchamp, *J. Am. Chem. Soc.* **1989**, *111*, 75 – 85.
[50] J. D. Burley, K. M. Ervin, P. B. Armentrout, *Int. J. Mass Spectrom. Ion Processes* **1987**, *80*, 153 – 175.
[51] T. Baer, W. L. Hase, *Unimolecular Reaction Dynamics: Theory and Experiments*, Oxford University Press, New York, **1996**.
[52] C. Rue, P. B. Armentrout, I. Kretzschmar, D. Schroder, J. N. Harvey, H. Schwarz, *J. Chem. Phys.* **1999**, *110*, 7858 – 7870.
[53] P. B. Armentrout in *Adv. Gas Phase Ion Chem. Vol. 1* (Eds.: N. Adams, L. M. Babcock), JAI Press, Greenwich, **1992**, pp. 83 – 119.
[54] C. S. Hinton, M. Citir, P. B. Armentrout, *J. Chem. Phys.* **2011**, *135*, 234302.
[55] G. Ohanessian, M. J. Brusich, W. A. Goddard III, *J. Am. Chem. Soc.* **1990**, *112*, 7179 – 7189.
[56] T. Leininger, J. F. Riehl, G. H. Jeung, M. Pelissier, *Chem. Phys. Lett.* **1993**, *205*, 301 – 305.
[57] X. Zhang, H. Schwarz, *Chem. Eur. J.* **2010**, *16*, 5882 – 5888.
[58] C. Y. Peng, H. B. Schlegel, *Isr. J. Chem.* **1993**, *33*, 449 – 454.
[59] C. Y. Peng, P. Y. Ayala, H. B. Schlegel, M. J. Frisch, *J. Comput. Chem.* **1996**, *17*, 49 – 56.
[60] A. Simon, J. Lemaire, P. Boissel, P. Maître, *J. Chem. Phys.* **2001**, *115*, 2510 – 2518.
[61] K. Yoshizawa, Y. Shiota, T. Yamabe, *J. Chem. Phys.* **1999**, *111*, 538 – 545.
[62] C. Heinemann, R. Wesendrup, H. Schwarz, *Chem. Phys. Lett.* **1995**, *239*, 75 – 83.
[63] U. Achatz, M. Beyer, S. Joos, B. S. Fox, G. Niedner-Schatteburg, V. E. Bondybey, *J. Phys. Chem. A* **1999**, *103*, 8200 – 8206.
[64] M. Pavlov, M. R. A. Blomberg, P. E. M. Siegbahn, R. Wesendrup, C. Heinemann, H. Schwarz, *J. Phys. Chem. A* **1997**, *101*, 1567 – 1579.
[65] Y.-M. Chen, P. B. Armentrout, *J. Am. Chem. Soc.* **1995**, *117*, 9291 – 9304.
[66] P. B. Armentrout, Y.-M. Chen, *J. Am. Soc. Mass Spectrom.* **1999**, *10*, 821 – 839.
[67] J. L. Elkind, P. B. Armentrout, *J. Phys. Chem.* **1986**, *90*, 5736 – 5745.
[68] E. R. Fisher, R. H. Schultz, P. B. Armentrout, *J. Phys. Chem.* **1989**, *93*, 7382 – 7387.
[69] R. H. Schultz, P. B. Armentrout, *Organometallics* **1992**, *11*, 828 – 836.
[70] Y.-M. Chen, J. L. Elkind, P. B. Armentrout, *J. Phys. Chem.* **1995**, *99*, 10438 – 10445.
[71] S. K. Loh, D. A. Hales, L. Lian, P. B. Armentrout, *J. Chem. Phys.* **1989**, *90*, 5466 – 5485.
[72] R. H. Schultz, P. B. Armentrout, *Int. J. Mass Spectrom. Ion Processes* **1991**, *107*, 29 – 48.
[73] E. Teloy, D. Gerlich, *Chem. Phys.* **1974**, *4*, 417 – 427.
[74] D. Gerlich, *Adv. Chem. Phys.* **1992**, *82*, 1 – 176.
[75] P. J. Chantry, *J. Chem. Phys.* **1971**, *55*, 2746 – 2759.
[76] C. Lifshitz, R. L. C. Wu, T. O. Tiernan, D. T. Terwilliger, *J. Chem. Phys.* **1978**, *68*, 247 – 260.
[77] B. L. Kickel, P. B. Armentrout, *J. Am. Chem. Soc.* **1995**, *117*, 4057 – 4070.
[78] D. E. Clemmer, Y.-M. Chen, F. A. Khan, P. B. Armentrout, *J. Phys. Chem.* **1994**, *98*, 6522 – 6529.
[79] C. L. Haynes, P. B. Armentrout, *Organometallics* **1994**, *13*, 3480 – 3490.
[80] B. L. Kickel, P. B. Armentrout, *J. Am. Chem. Soc.* **1995**, *117*, 764 – 773.
[81] M. R. Sievers, Y.-M. Chen, J. L. Elkind, P. B. Armentrout, *J. Phys. Chem.* **1996**, *100*, 54 – 62.
[82] C. E. Moore, *Atomic Energy Levels*, *NSRDS-NBS 35*, Washington, D.C., **1971**.
[83] T. A. M. Van Kleef, P. F. A. Klinkenberg, *Physica* **1961**, *27*, 83 – 94.
[84] W. J. Chesnavich, M. T. Bowers, *J. Chem. Phys.* **1978**, *68*, 901 – 910.
[85] N. Aristov, P. B. Armentrout, *J. Am. Chem. Soc.* **1986**, *108*, 1806 – 1819.
[86] T. Shimanouchi, *NSRDS-NBS* **1972**, *39*, 1.
[87] A. D. Becke, *J. Chem. Phys.* **1993**, *98*, 5648 – 5652.
[88] C. Lee, W. Yang, R. G. Parr, *Phys. Rev. B* **1988**, *37*, 785 – 789.
[89] Gaussian 09, Revision A.02, M. J. Frisch, G. W. Trucks, H. B. Schlegel, G. E. Scuseria, M. A. Robb, J. R. Cheeseman, G. Scalmani, V. Barone, B. Mennucci, G. A. Petersson, H. Nakatsuji, M. Caricato, X. Li, H. P. Hratchian, A. F. Izmaylov, J. Bloino, G. Zheng, J. L. Sonnenberg, M. Hada, M. Ehara, K. Toyota, R. Fukuda, J. Hasegawa, M. Ishida, T. Nakajima, Y. Honda, O. Kitao, H. Nakai, T. Vreven, J. A. Montgomery, Jr., J. E. Peralta, F. Ogliaro, M. Bearpark, J. J. Heyd, E. Brothers, K. N. Kudin, V. N. Staroverov, R. Kobayashi, J. Normand, K. Raghavachari, A. Rendell, J. C. Burant, S. S. Iyengar, J. Tomasi, M. Cossi, N. Rega, J. M. Millam, M. Klene, J. E. Knox, J. B. Cross, V. Bakken, C. Adamo, J. Jaramillo, R. Gomperts, R. E. Stratmann, O. Yazyev, A. J. Austin, R. Cammi, C. Pomelli, J. W. Ochterski, R. L. Martin, K. Morokuma, V. G. Zakrzewski, G. A. Voth, P. Salvador, J. J. Dannenberg, S. Dapprich, A. D. Daniels, O. Farkas, J. B. Foresman, J. V. Ortiz, J. Cioslowski, D. J. Fox, Gaussian Inc., Pittsburgh, PA, **2009**.
[90] D. Andrae, U. Haeussermann, M. Dolg, H. Stoll, H. Preuss, *Theor. Chim. Acta* **1990**, *77*, 123 – 141.
[91] F. Weigend, R. Ahlrichs, *Phys. Chem. Chem. Phys.* **2005**, *7*, 3297 – 3305.
[92] D. Feller, *J. Comput. Chem.* **1996**, *17*, 1571 – 1586.
[93] K. L. Schuchardt, B. T. Didier, T. Elsethagen, L. Sun, V. Gurumoorthi, J. Chase, J. Li, T. L. Windus, *J. Chem. Inf. Model.* **2007**, *47*, 1045 – 1052.
[94] M. C. Holthausen, M. Mohr, W. Koch, *Chem. Phys. Lett.* **1995**, *240*, 245 – 252.
[95] F. Furche, J. P. Perdew, *J. Chem. Phys.* **2006**, *124*, 044103.
[96] T. G. Rowland, B. Sztáray, P. B. Armentrout, *J. Phys. Chem. A* **2013**, *117*, 1299 – 1309.
[97] C. S. Hinton, M. Citir, P. B. Armentrout, *Int. J. Mass Spectrom.* **2013**, DOI: 10.1016/j.ijms.2013.05.015.
[98] D. Dai, K. Balasubramanian, *Chem. Phys. Lett.* **1991**, *185*, 165 – 171.
[99] M. Benavides-Garcia, K. Balasubramanian, *J. Mol. Spectrosc.* **1991**, *150*, 271 – 279.
[100] R. S. Ram, J. Lievin, P. F. Bernath, *J. Chem. Phys.* **1999**, *111*, 3449 – 3456.
[101] M. A. Garcia, M. D. Morse, *J. Chem. Phys.* **2011**, *135*, 114304.
[102] H. Lefebvre-Brion, R. W. Field, *The Spectra and Dynamics of Diatomic Molecules*, Elsevier, Amsterdam, **2004**.

Received: April 22, 2013
Published online on August 19, 2013

This paper is part of a Special Issue dedicated to the memory of Detlef Schröder. To view the complete issue, visit: http://onlinelibrary.wiley.com/doi/10.1002/cplu.v78.9/issuetoc